The background of the cover is a grayscale image of a scanning probe microscope (SPM) tip. The tip is a sharp, conical structure with a textured surface, showing concentric rings of material. It is positioned in the lower center of the frame, pointing downwards. The background is dark, making the tip stand out.

Department of Precision and Microsystems Engineering

Hamaker constant and tip radius determination in dynamic atomic force microscopy

Matthew James (4712498)

Report no : 2019.032
Coach : Ir. Abhilash Chandrashekar, Dr. Pierpaolo Belardinelli
Professor : Dr. Farbod Alijani
Specialisation : Dynamics of Micro and Nanosystems
Type of report : Master Thesis
Date : 30 September 2019

Hamaker constant and tip radius determination in dynamic atomic force microscopy

MASTER OF SCIENCE THESIS

For the degree of Master of Science in High Tech Engineering at
Delft University of Technology

Matthew James

30 September, 2019

Faculty of Mechanical, Maritime and Materials Engineering (3mE) ·
Delft University of Technology

Abstract

Atomic Force Microscopy (AFM) is an extremely powerful tool for exploring surface topology and nanoscale manipulation and characterization. A feature of AFM is the existence of highly nonlinear forces between a cantilever tip and sample. One of these forces that plays a large role in operation of AFM is the Van der Waals (VdW) force. This force is characterized in part by the Hamaker constant H and cantilever tip radius R . Measuring these two properties quickly and accurately can facilitate further characterization methods in dAFM.

This research will focus on creating methods in which H and R can be extracted using the dynamic response of a cantilever. The VdW force is used to extract H by analyzing the softening behavior of Frequency Response Curves (FRCs). Electrostatic forces are used to extract R by applying a simplified Kelvin Probe Force Microscopy (KPFM) technique. The method proposed to extract H was demonstrated numerically, but technical limitations prevented an experimental proof of the method. The method to extract R was proven experimentally and validated using a Scanning Electron Microscopy (SEM) image.

Table of Contents

1	Introduction	1
1-1	Background	1
1-1-1	Hamaker constant	3
1-2	Force models	3
1-2-1	Hertz force model	4
1-2-2	DMT force model	4
1-2-3	Electrostatic forces	5
1-3	Cantilever dynamics in AFM	6
1-4	Frequency Response Curve	8
1-5	Analytical theory	10
1-6	Operational modes of AFM	11
1-6-1	AM AFM	12
1-6-2	FM AFM	12
1-6-3	KPFM	13
1-7	Measuring Hamaker constant	13
1-7-1	Lifshitz theory	13
1-7-2	Static AFM	14
1-7-3	Quasi-dynamic AFM	14
1-8	Measuring the tip radius	15
1-8-1	Force vs static gap	15
1-8-2	DC voltage vs static gap	16
1-9	Conclusion	16
2	Hamaker constant determination using Frequency Response Curves in Atomic Force Microscopy	19
3	Tip radius determination using a simplified Kelvin Probe Force Microscopy technique	29
4	Conclusion & Recommendations	35
4-1	Conclusion	35
4-2	Recommendations	36
4-2-1	Analytical Equation to model Hardening	36
4-2-2	Technical Solutions to extracting the Hamaker constant	36
4-2-3	Real time tip radius identification	37

Appendices	39
A	41
A-1 Method of Averaging	41
A-1-1 Simplified Van der Waals force	41
A-1-2 General Van der Waals force	43
A-2 Sheared fitting function	44
A-3 Numerical Simulations	44
A-4 Experiments	49
A-5 Non dimensionalized amplitude methods and phase	50
A-5-1 MLA sensitivity	50
A-5-2 Nanosurf Sensitivity	50
A-5-3 Amplitude Ratio	51
A-5-4 Phase	51
A-5-5 Experiment Discussion	52
A-6 Experimental FRC fits	53
A-7 Humidity affects on experiments	60
B	61
B-1 Capacitance gradient analytical model	61
C	63
C-1 Cantilever dynamics Theory	63

Chapter 1

Introduction

The Atomic Force Microscope (AFM) was invented in 1982 as a way to provide a quantitative map of surface topography with atomic resolution [1]. Since then, the field has expanded dramatically, in large due to the invention of dynamic AFM (dAFM) and its two sub modes of operation; Amplitude Modulated AFM (AM-AFM) and Frequency Modulated AFM (FM-AFM). These modes of operation are a powerful and versatile technique for atomic and nanometer scale characterization and manipulation of a wide variety of surfaces [2]. Taken together, these developments have led to the widespread use of AFM in all fields of science and engineering [3]. In particular, the nonlinear nature of AFM is increasingly being used and measured to reveal specific properties of the tip and sample.

This thesis consists of three parts. Firstly, this chapter summarizes existing AFM literature. It covers the basics behind AFM operation, and briefly elaborates on the existing methods that are currently being used to extract H and R . The second chapter includes two papers which summarize the methods proposed to extract H and R respectively. The last chapter includes a conclusion and recommendation. A collection of supplementary material has been provided in the appendix.

1-1 Background

AFMs feature a micro cantilever with a sharp tip at its free end close to the surface of a sample where multiple strongly nonlinear forces are present. These nonlinear tip-sample interaction forces F_{ts} can be either conservative or dissipative in nature, and are often

strongly dependant on the instantaneous tip sample separation d .

Simplified models of these tip sample interaction forces have been made, many of which have been derived assuming a spherical tip interacting with a perfectly flat surface [3,4].

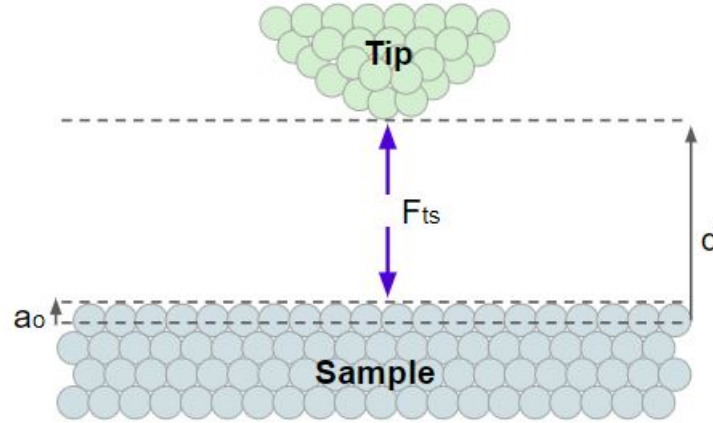


Figure 1-1: Tip and sample figure. d is the instantaneous tip sample separation, F_{ts} is the tip sample interaction force at this distance, and a_0 is the inter molecular distance.

Most of these force models have analytical expressions which clearly distinguish between contact and non contact regions. Contact is defined when the tip-sample gap is less than or equal to the inter molecular distance $d \leq a_0$, and non contact is defined when $d > a_0$.

Likewise, a few of these models account for the attractive Van der Waals force F_{VDW} which is derived from Keesom, Debye and London potential energies and integrating over a continuum of a sphere (the tip) and a plane (the sample). The general expression for the force becomes

$$F_{VDW} = -\frac{2HR^3}{3d^2(2R+d)^2} \quad (1-1)$$

Where H is the Hamaker constant and R is the tip radius.

However, for the case where the tip radius is sufficiently larger than the instantaneous tip sample separation $R \gg d$ then this expression can be simplified to

$$F_{VDW} = -\frac{HR}{6d^2} \quad (1-2)$$

Despite being considered a long range force, the VdW force typically only has an influence at around a few nanometers or less [5,6]. However, at larger distances retardation effects

due to the finite speed of light become apparent and give rise to a Casimir force [5]. This retardation effect causes the force to fall more rapidly with distance than the traditional VdW force, and even change sign. However this typically happens outside of the range of traditional AFM [4].

1-1-1 Hamaker constant

The Hamaker constant is a measure of the strength of the VdW force and varies depending on the media that make up the tip and sample, and the medium it interacts across [7]. The Hamaker constant for media 1 and 2 interacting across medium 3, H_{132} , is given by equation 1-3

$$H_{132} \approx (\sqrt{H_{11}} - \sqrt{H_{33}})(\sqrt{H_{22}} - \sqrt{H_{33}}) \quad (1-3)$$

Where H_{ij} is the Hamaker constant for media i interacting across a vacuum with media j . This equation approximates poorly, however, when applied to media with high dielectric constants such as water. Nonetheless, the Hamaker constant is typically 5-10 times less across water than the Hamaker constant across air/vacuum [8]. This means the VdW force can gradually be reduced as water condenses in between the gap between the tip and sample.

Table 1-1: Table of Hamaker constants for different materials interacting across a medium of air or water [7, 9–14]

Hamaker constant $H_{132}(10^{-20}J)$	Media		
	1	3	2
6.3	SiO ₂	air	SiO ₂
18.63	Silicon	air	Silicon
9.86	Mica	air	Mica
47	HOPG	air	HOPG
45.5	Gold	air	Gold
29.6	Silicon	air	HOPG
40	Silver	air	Silver
2.01	Mica	water	Mica
9.75	Silicon	water	Silicon
11.5	HOPG	water	HOPG

1-2 Force models

Many different force models exist to approximate the true tip sample interaction force. Some force models are more appropriate than others based on the type of material that constitutes the tip and sample, and the expected applied load during measurement [3,15].

Two of these force models are the Hertz force model, and the Derjaguin-Muller-Toporov (DMT) force model.

1-2-1 Hertz force model

The Hertz force model is a relatively simple contact model because it neglects the existence of any attractive forces, including the VdW force. The key assumptions behind this model include negligible adhesion, small tip radius and no long range forces.

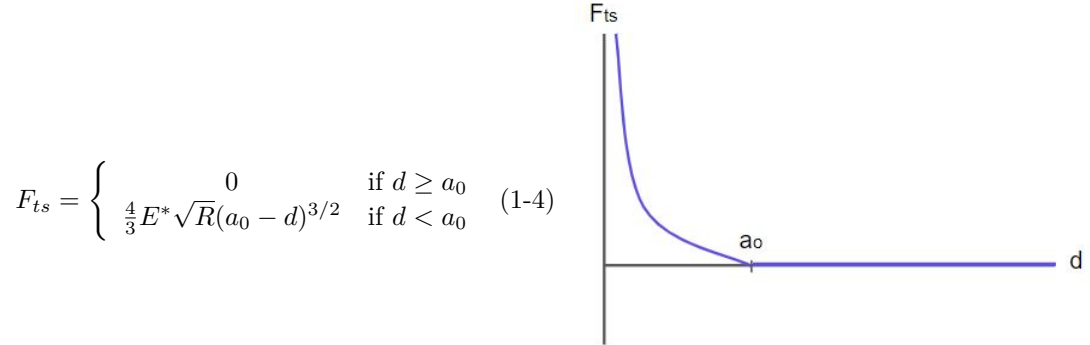


Figure 1-2: Hertz force model

Where R is the tip radius, H is the Hamaker constant, a_0 is the inter molecular distance and E^* is the effective Young's modulus. ν is the Poisson ratio and E is the Young's modulus.

$$E^* = \left(\frac{1 - \nu_{tip}^2}{E_{tip}} + \frac{1 - \nu_{sample}^2}{E_{sample}} \right)^{-1}$$

1-2-2 DMT force model

The DMT contact model is commonly used because it is a hybrid consisting of both Hertz contact forces and long range Van der Waals (VDW) forces. The long range VdW forces use the simplified expression given in equation 1-2 [3]. This contact model is convenient to use since it is a conservative force model, implying there are no dissipative nonlinear tip sample forces that can lead to hysteresis. However, similar to the Hertz contact model, it is not differentiable at a_0 , making it also quite challenging to analyze numerically. This model assumes low adhesion and hard substrates [2].

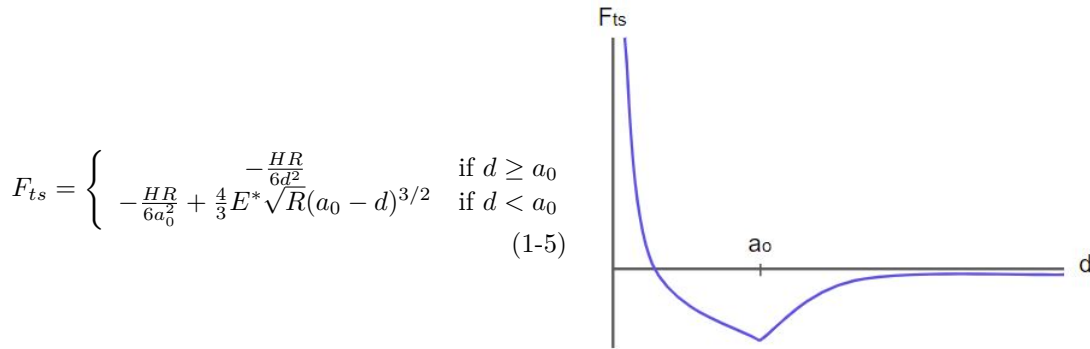


Figure 1-3: DMT force model

1-2-3 Electrostatic forces

Electrostatic forces arise from quantum mechanical phenomena whereby electrons tunnel from a sharp metallic tip to a sufficiently conductive substrate. This essentially creates a capacitor between the tip and sample which results in an adhesive force. Electrostatic forces typically have the largest strength and longest range [16]. The long range electrostatic force can be measured and mitigated by using Kelvin Probe Force Microscopy (KPFM) which creates a bias voltage, nullifying the capacitor [3, 17]. In general the electrostatic force that exists between a static tip and sample can be written as

$$F_{elec} = -\frac{1}{2} \frac{dC}{dz} \Delta V^2 \quad (1-6)$$

Where ΔV is the potential difference between the tip and sample, C is the capacitance, and z is the static tip sample gap between the tip and sample. Since the capacitance is largely a function of the geometry of the cantilever, there are many different models for the electrostatic force between the tip and sample [17, 18]. However, a complete analytical formula has been outlined in the appendix B, which breaks the components of capacitance gradient into 3 separate regions; the tip apex, tip cone and cantilever base. The total capacitance is the sum of all 3 components [16].

$$\frac{dC}{dz} = \frac{dC}{dz}_{apex} + \frac{dC}{dz}_{cone} + \frac{dC}{dz}_{lever} \quad (1-7)$$

The apex term tends to dominate at low gaps between tip and sample, whereas the cone and lever components tend to dominate at large gaps [17]. Lately, however, more attention is being put towards modelling the whole cantilever - tip system numerically, rather than analytically [19].

1-3 Cantilever dynamics in AFM

In dynamic AFM (dAFM) the cantilever is intentionally exposed to additional external forces which make the cantilever vibrate. There are two popular methods of excitation; acoustic and magnetic. In acoustic excitation, a piezoactuator in contact with the micro-cantilever chip holder drives its oscillation. In magnetic excitation, an oscillating magnetic field beneath the sample drives cantilever oscillation [20]. These methods will produce theoretically different Frequency Response Curves (FRC's), however these differences can only be observed for low cantilever stiffness k and quality factor Q . For high k or high Q the differences become negligible [20]. Figure 1-4 illustrates the various defined positions of the cantilever while undergoing acoustic excitation.

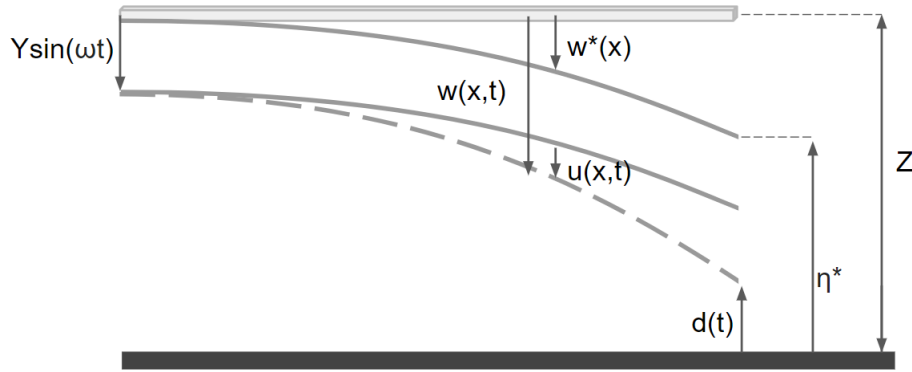


Figure 1-4: Cantilever Deflection configurations under acoustic excitation. In order from top to bottom; undeflected, static deflection, static deflection + base excitation, instantaneous displacement

$w^*(x)$ denotes the static displacement of the cantilever without any external excitation, $Y \sin(\omega t)$ denotes the base excitation from the piezo, $w(x, t)$ is the absolute instantaneous position of the cantilever and $u(x, t)$ is the instantaneous position of the cantilever relative to base excitation and static deflection. $d(t)$ is the instantaneous tip sample gap, η^* is the static deflection tip sample gap, and Z is the undeflected, unforced position of the cantilever tip sample gap.

The dynamics of the cantilever can be well approximated using Euler-Bernoulli Beam theory. In this formula $f(x)$ is the external force per unit length acting on the cantilever. Since a positive tip sample force is a point force that is considered repulsive by convention $f(x) = -F_{ts}\delta(x - L)$ [12, 21, 22].

$$\begin{aligned} \rho A \ddot{w}(x, t) + EI w''''(x, t) &= f(x) \\ \rho A \ddot{u}(x, t) + EI (u''''(x, t) + w^{*''''}(x)) &= -F_{ts}(\eta^* - u(L, t) - Y \sin \omega t) \delta(x - L) + \omega^2 \rho A Y \sin \omega t \end{aligned} \quad (1-8)$$

Solving this equation of motion for $u(x, t)$ is difficult due to the presence of nonlinearities. However, the cantilever tip can be accurately modelled as a single degree of freedom

(SDoF) spring mass damper instead, so long as it's oscillating near it's first natural frequency. By using Euler Bernoulli beam theory it can be proven (as shown appendix chapter C-1) that the equivalent spring stiffness and equivalent mass of this 1 DoF system is

$$k = \frac{3EI}{L^3}$$

$$m \approx 0.242m_c$$

Where E is the youngs modulus, I is the moment of inertia, L is the length, and $m_c = \rho AL$ is the mass of the cantilever.

The excitation of the whole cantilever caused by the piezo can be accounted for by modelling the 1 DoF system as if both a base and mass are undergoing harmonic excitation. An additional damper is added which is to account for several (largely unknown) dissipative interactions. The equation that governs this motion is described below. Note that

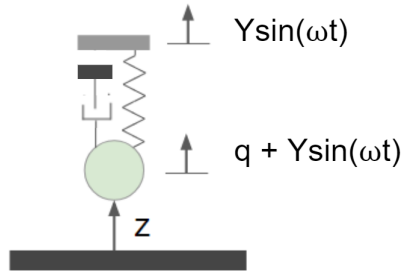


Figure 1-5: 1 DoF base excitation model of cantilever tip

the natural frequency far from the sample is $\omega_0 = \sqrt{\frac{k}{m}}$ and the quality factor far from the sample is $Q = \frac{m\omega_0}{c}$. The equation can also be nondimensionalized by introducing nondimensionalized time and displacement $\tau = \omega_0 t$ and $x = \frac{q}{z}$. The nondimensionalized equation of motion is also presented in 3D state space.

$$m\ddot{q} + c\dot{q} + kq = m\omega^2 Y \sin(\omega t) - c\omega Y \cos(\omega t) + F_{ts}(z + q + Y \sin \omega t)$$

$$x'' + \frac{1}{Q}x' + x = \left(\frac{\omega}{\omega_0}\right)^2 \frac{Y}{z} \sin\left(\frac{\omega}{\omega_0}\tau\right) - \frac{\omega}{\omega_0} \frac{Y}{z} \frac{1}{Q} \cos\left(\frac{\omega}{\omega_0}\tau\right) + \frac{F_{ts}(z + zx + Y \sin \frac{\omega}{\omega_0}\tau)}{zk}$$

$$\begin{pmatrix} x' \\ y' \\ Z' \end{pmatrix} = \begin{pmatrix} (\frac{\omega}{\omega_0})^2 \frac{Y}{z} \sin(Z) - \frac{\omega}{\omega_0} \frac{Y}{z} \frac{1}{Q} \cos(Z) + \frac{F_{ts}}{zk} - \frac{1}{Q}y - x \\ y \\ \frac{\omega}{\omega_0} \end{pmatrix} \quad (1-9)$$

The equation of motion shown in equation 1-9 was derived using harmonic base excitation, however many authors simplify this expression and assume the equation of motion has the form of simple point excitation instead [2]. The following equations shows the equation of motion for point excitation, the non dimensionalized equation of motion (using $\tau = t\omega_0$ and $x = \frac{q}{z}$) and the non dimensionalized equation of motion in state space form.

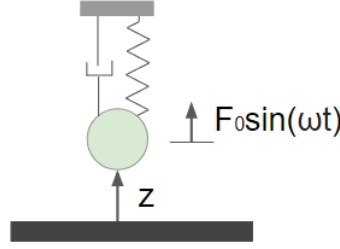


Figure 1-6: 1 DoF point excitation model of cantilever tip

$$\begin{aligned}
 \ddot{q} + \frac{\omega_0}{Q} \dot{q} + \omega_0^2 q &= \frac{F_0}{m} \sin(\omega t) + \frac{F_{ts}(z + q)}{m} \\
 x'' + \frac{1}{Q} x' + x &= \frac{F_0}{kz} \sin\left(\frac{\omega}{\omega_0} \tau\right) + \frac{F_{ts}(z + zx)}{kz} \\
 \begin{pmatrix} x' \\ y' \\ Z' \end{pmatrix} &= \begin{pmatrix} \frac{F_0}{kz} \sin(Z) + \frac{y}{kz} - \frac{1}{Q} y - x \\ \frac{\omega}{\omega_0} \end{pmatrix}
 \end{aligned} \tag{1-10}$$

1-4 Frequency Response Curve

The Frequency Response Curve (FRC) is a compact way of expressing the steady state amplitude of the cantilever tip A over a range of drive frequencies ω . In the absence of tip sample interaction forces, the FRC is linear showing a single, vertical peak in amplitude at its natural frequency. However, due to the presence of the highly nonlinear tip sample interaction forces, the FRC begins to curve, creating complicated hysteric dynamics. A complete analytical expression for the FRC is not possible, however an approximate model assuming only the presence of the Van der Waals force (VdW) is derived in the appendix in section A-1.

It's important to notice that the FRC is strongly dependant on the static tip sample gap z and strength of excitation F_0 . Since F_{ts} approaches 0 at large distances from the sample, the FRC will look linear at large z and will be governed by the following amplitude and phase equations.

$$\begin{aligned}
 A_{far} &= \frac{F_0}{k} \frac{1}{\sqrt{\left(1 - \left(\frac{\omega}{\omega_0}\right)^2\right)^2 + \left(\frac{1}{Q} \frac{\omega}{\omega_0}\right)^2}} \\
 \alpha_{far} &= \tan^{-1} \left(\frac{\frac{\omega}{\omega_0}}{Q \left(1 - \left(\frac{\omega}{\omega_0}\right)^2\right)} \right)
 \end{aligned} \tag{1-11}$$

Where A_{far} and α_{far} is the amplitude and phase of the tip far from the surface, Q is the quality factor and $\frac{\omega}{\omega_0}$ is the nondimensionalized excitation frequency. However, for experiments in which the tip is significantly close to the sample (but still not in contact), the presence of the nonlinear attractive forces will make the FRC undergo a softening behavior in which the FRC amplitude peak and corresponding phase curves left. This implies that the natural frequency decreases while oscillating in the attractive regime. This is mainly because the attractive forces effectively act to decrease stiffness of the system in this regime.

Likewise, if the tip gets even closer to the sample such that it is in contact, then the large repulsive forces will cause the FRC to undergo a hardening behavior in which the FRC amplitude peak and corresponding phase curves right. This is mainly because the tip sample interaction force effectively increases stiffness of the system in this regime.

For these nonlinear curves to be noticed, either the static tip sample gap z needs to be sufficiently close to the sample, or the external forcing of the cantilever needs to be large enough to cause the tip to dip close enough to the sample during its oscillation.

Figure 1-7 shows a typical FRC calculated using a point excitation model from equation 1-10 [23]. It demonstrates the influence additional forcing and static tip sample gap can have on the FRC. Both can experience softening and hardening behavior if the forcing is sufficiently large or the static tip sample gap is sufficiently small.

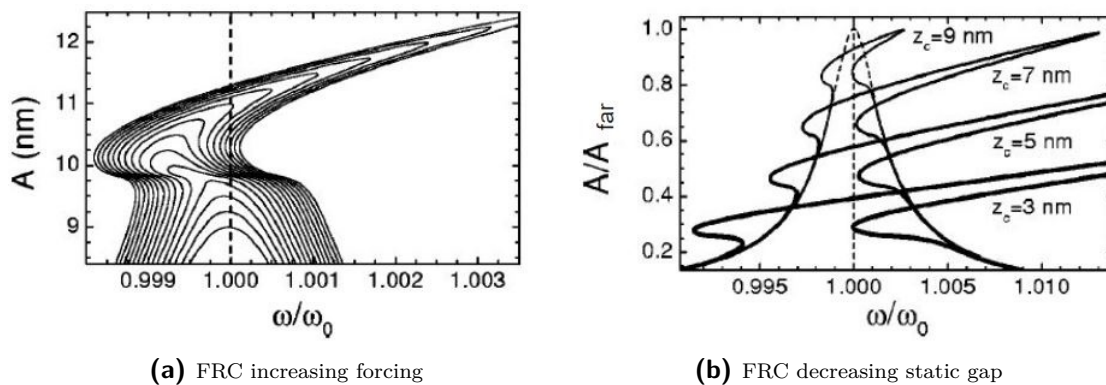


Figure 1-7: FRCs calculated using point excitation model. Figure 1-7a increases forcing while fixing static displacement ($z = 10\text{nm}$). This shows the transition from linear to softening to hardening behavior. Figure 1-7b decreases static gap while fixing forcing ($A_{far} = 11\text{nm}$) [23].

As shown in figure 1-7, there are a range of drive frequencies for which multiple amplitudes are possible. This can be understood more completely through the use of a 2D phase space diagram which capture the transient and steady state motion of the tip oscillation visually. Since FRCs only feature steady state information, the amplitude of the FRC at a specific drive frequency corresponds to the maximum displacement of a limit cycle (ie periodic solution) - and all transient motion between these limit cycles is

neglected. If an excitation frequency has multiple corresponding amplitudes, then this implies the existence of multiple stable/ unstable limit cycles. Limit cycles that are unstable will correspond to an amplitude point which lies on an unstable amplitude branch. Consequently, these branches are impossible to see naturally through experiment.

Due to the presence of unstable amplitude branches, a hysteretic nature can be observed during a frequency sweep whenever an unstable saddle node bifurcation is reached. On the onset of hitting an unstable limit cycle, the amplitude will instantly spike up/down to the nearest stable amplitude. This jump in amplitude will be different for forward frequency sweeps and backward frequency sweeps leading to path dependant behavior.

1-5 Analytical theory

Recent theoretical strides have allowed the motion of the AFM tip to be well approximated by analytical formulas. By introducing two new variables; the Virial V_{ts} and the Energy Dissipation E_{ts} , and making a few reasonable assumptions, some valuable expressions and intuitions can be gained.

Firstly, even though a harmonic base excitation equation of motion is more accurate, a more simple force excitation model is assumed. The tip sample force has also been deconstructed into conservative (also known as path independent since the force only depends on the distance between the tip and sample, not the path taken to get there) and dissipative (also known as path dependant) parts $F_{ts} = F_{ts,cons} + F_{ts,diss}$.

$$\frac{1}{\omega_0^2} \ddot{q} + \frac{1}{\omega_0 Q} \dot{q} + q = \frac{F_0}{k} \sin \omega t + \frac{1}{k} (F_{ts,cons} + F_{ts,diss}) \quad (1-12)$$

Where F_0 is the excitation force. Despite nonlinear components of force, it is assumed that the steady state displacement of the tip is purely sinusoidal $q = A \sin(\theta)$ where $\theta = \omega t - \alpha$. Also, at some fixed static gap z , the conservative force applied back on the tip due to the sinusoidal motion around z can be assumed to be some even function vs θ (since it is path independent), whereas the dissipative force can be assumed to be some odd function (since it is path dependant and acts in a direction that opposes the velocity of the tip). The Virial V_{ts} and Energy Dissipation E_{ts} are defined by the following relations.

$$\begin{aligned} V_{ts} = \langle F_{ts,cons} q \rangle &= \frac{1}{2\pi} \int_0^{2\pi} q \times F_{ts,cons} d\theta \\ &= \frac{kA^2}{2} \left(1 - \frac{\omega^2}{\omega_0^2}\right) - \frac{AF_0}{2} \cos \alpha \end{aligned} \quad (1-13)$$

$$\begin{aligned}
E_{ts} &= - \langle F_{ts,diss} q \rangle = - \frac{1}{2\pi} \int_0^{2\pi} q \times F_{ts,diss} d\theta \\
&= \pi A F_0 \sin \alpha - \frac{\pi k A^2 \omega}{Q \omega_0}
\end{aligned} \tag{1-14}$$

The Virial V_{ts} can be thought of as the negative of stored energy in the conservative tip sample interaction, whereas the Energy Dissipation E_{ts} can be thought of as the irreversible work done in one oscillation cycle by the tip on the sample. Using equations 1-13 and 1-14 and eliminating α , relationships for the nonlinear natural frequency ω'_0 and quality factor Q' at some fixed static gap z can be found.

$$\begin{aligned}
\omega'_0 &= \omega_0 - \omega_0 \frac{V_{ts}}{kA^2} \\
Q' &= \left(\frac{1}{Q} + \frac{\omega_0 E_{ts}}{\omega \pi k A^2} \right)^{-1}
\end{aligned} \tag{1-15}$$

Likewise, the amplitude reduction (also called setpoint) and phase can be found for the case where the tip is oscillating near resonance. The amplitude reduction $\frac{A}{A_{far}}$ is the ratio of the amplitude of steady state oscillation at some static gap z to the steady state amplitude sufficiently far away from the sample such that tip sample forces can be neglected. Formulas for the amplitude reduction and steady state phase are outlined in equations 1-16 and 1-17.

$$\frac{A}{A_{far}} = \frac{\frac{1}{Q}}{\sqrt{(-2 \frac{V_{ts}}{kA^2})^2 + (\frac{1}{Q} + \frac{E_{ts}}{\pi k A^2})^2}} \tag{1-16}$$

$$\tan \alpha = \frac{\frac{1}{Q} + \frac{E_{ts}}{\pi k A^2}}{-2 \frac{V_{ts}}{kA^2}} \tag{1-17}$$

1-6 Operational modes of AFM

As discussed in section 1-5, the amplitude, phase shift and natural frequency of the cantilever change as the cantilever is slowly made to move toward or away from the surface. This fact can be exploited to scan the topography of the surface through the use of a feedback controller. Two different styles of controlling the system are Amplitude Modulated AFM (AM AFM) and Frequency Modulated AFM (FM AFM). These

techniques are different in operation but can both be used to measure the topography of a sample. Lock in Amplifiers (LIA) are used in all dAFM's. Their purpose is to detect the amplitude and phase of the cantilever accurately during measurement. In reality the signal recorded from the photo diode will contain noise and higher harmonics which is not desired (unless using multifrequency AFM). It's possible to lock on to a single frequency (normally the driving frequency) to extract useful data by integrating out the other data over a sufficiently long time. In addition to this authors have also suggested the design of multiple frequency LIA's [24]. Phase Locked Loops (PLL) are commonly used in FM AFM to keep a system at resonance, which occurs when the excitation force is approximately 90° out of phase with the steady state displacement of the cantilever. To do this, the PLL acts as a controller that works in tandem with a LIA to get a feedback value for the phase so that it can be controlled to be 90° .

1-6-1 AM AFM

Information about the position of the cantilever is measured by shining a laser on the end of the cantilever as it's in motion. The laser reflects from the cantilever to a 4 quadrant photo diode which records instantaneous relative displacement. The feedback loop of the controller can adjust multiple parameters including drive excitation force, excitation frequency and base height of the cantilever in order to keep the static tip sample gap z a fixed distance above the topography of the sample. In AM AFM (also called tapping mode AFM), the amplitude A of the tip is controlled to be constant by adjusting the static displacement of the cantilever z . To do this, the drive frequency ω and forcing F_0 is kept constant so that any changes in the amplitude are purely a result of tip sample gap differences caused by changes in topography as the tip scans the surface. Clearly the displacement of the cantilever to maintain constant amplitude must be effectively equal to the relative height of the sample, hence creating 1D topography scan. This process is repeated multiple times, scanning hundreds/thousands of lines across a rectangular area of the sample. A powerful advantage of AM AFM is that the phase (which has been left to vary) provides additional data which can be used to find material properties.

1-6-2 FM AFM

In FM AFM, the natural frequency of the cantilever ω_n (which can change due to the presence of nonlinear forces) is controlled to be constant by adjusting the static displacement of the cantilever z . Multiple feedback loops are included which make sure that the drive frequency always matches the natural frequency - which implies maintaining resonance where the phase lag = 90° . And the amplitude remains constant by adjusting the force excitation F_0 . Since the amplitude and phase is controlled to be constant, any change in natural frequency (also called frequency shift $\Delta\omega_n$) must be a result of changes in the topography as the tip scans the surface. Just like AM AFM, the the displacement of the cantilever effectively maps the relative topography height. A powerful advantage to this mode of operation is the increased sensitivity without any restriction to bandwidth due to constantly exciting the cantilever at resonance [2].

1-6-3 KPFM

KPFM is another operation mode of AFM. KPFM is a non contact technique for measuring the surface potential (or surface voltage V_s) of a sample [25, 26]. There are a few different variants of KPFM. One of these methods involves scanning the topography of a sample by exciting the cantilever mechanically at the first natural frequency. In addition to this, the cantilever is also excited electrically with a DC and AC tip voltage. This tip voltage will cause the electrostatic force to have components at three distinct frequencies. One of these components is presented in equation 1-18.

$$\begin{aligned}
 F_{elec0} &= -\frac{1}{2} \frac{dC}{dz} \left((V_s - V_{DC})^2 + \frac{1}{2} V_{AC}^2 \right) \\
 F_{elec1} &= \frac{dC}{dz} (V_s - V_{DC}) V_{AC} \sin(\omega_{elec} t) \\
 F_{elec2} &= \frac{1}{4} \frac{dC}{dz} V_{AC}^2 \cos(2\omega_{elec} t)
 \end{aligned} \tag{1-18}$$

Where V_s is the surface voltage, V_{DC} is the applied DC tip voltage, V_{AC} is the applied AC tip voltage, and ω_{elec} is the applied AC electrical frequency. As the tip moves along the surface, a separate LIA is used to output the amplitude and phase at ω_{elec} . A controller is then used to adjust V_{DC} such that the amplitude measured at the electrical excitation frequency is zero - effectively mitigating F_{elec1} . This DC voltage is known as the bias voltage because it perfectly matches the sample voltage to cancel out the electrostatic force. Consequently, this bias voltage is also a record of V_s at every point along the sample.

1-7 Measuring Hamaker constant

The Hamaker constant is a quantity that describes the strength of the attractive region of the VdW force between a spherical tip and a flat substrate. In the literature, there have been several ways this constant has been calculated or measured. Historically, H has been calculated theoretically using Lifshitz theory. But it can also be measured experimentally using a variety of techniques. Three of the most common ways of finding H have been outlined below.

1-7-1 Lifshitz theory

Theoretically H can be calculated using quantum electrodynamic Lifshitz theory. This theory takes into account the interaction potential energy from Keesom, Debye and London effects between all atoms that make up the tip and sample. By assuming a continuum model of the tip and surface, and assuming the tip radius is much larger than the tip-sample gap ($R \gg d$), the well known attractive component of the VDW force is derived to be $F(d) = -\frac{HR}{6d^2}$ where

$$H = \pi^2 \rho_1 \rho_2 C_{VDW} \quad (1-19)$$

Where C_{VDW} is a constant depending on the number density of atoms, the dipole moment, the polarizability, and I is the ionization energy.

Lifshitz theory is commonly used as the standard against which experimental methods are evaluated, it has some limitations which make direct experimental measurement preferable. Firstly a limitation of Lifshitz theory is that it doesn't rigorously characterize the collective nature of macroscopic dispersion interactions [27]. Also, the application of this formula is limited by the need for optical response data over a wide range of frequencies for the interacting materials, and this information is available only for a relatively small number of materials [28].

1-7-2 Static AFM

A simple way to measure H directly is to use static AFM. H can be measured by slowly lowering the cantilever until the tip snaps into contact. H is found by solving for when the tip sample force equals the restoring force, and when the slope of the interaction force equals the slope of the restoring force. The result is given by equation 1-20 [29].

These two equations can be solved simultaneously to find Hamaker constant in terms of the cantilever stiffness k , tip radius R and undeflected position of the cantilever when snap-in occurs z_{jump} [29].

$$H = \frac{8z_{jump}^3 k}{9R} \quad (1-20)$$

This formula for predicting H is limited due to the inherent flaws in Static AFM. Since the substrate and the cantilever must realistically approach each other with a non zero approach speed, the cantilever system is inherently dynamic. Likewise, the snap-in point only truly exists in the limit where the approach speed is 0, and cannot be reliably determined from an AFM static deflection curve. [28].

1-7-3 Quasi-dynamic AFM

The method proposed in subsection 1-7-2 H can be improved by using a "quasi-dynamic" method which improves upon the static method by accounting for finite times taken to snap into contact [30]. In practice there will always be some finite approach speed v_c between the tip and sample before snap-in, which makes the system is inherently dynamic. This complicates matters because for finite approach speeds a true jump point doesn't

appear and the amount the cantilever deflects during snap-in varies. Consequently, applying the static formula to an intrinsically dynamic system will only yield an apparent Hamaker constant H_{app} .

To solve for the true Hamaker constant H , the following method is applied. Firstly, the amount the cantilever is deflected once it has snapped into the surface Δd is calculated for a range of approach speeds. This is done by assuming the tip undergoes forced projectile motion without the presence of damping during snap-in. Next, the apparent Hamaker constant can be calculated at each value of Δd using the static AFM equation.

$$H_{app} = \frac{3k(\Delta d)^3}{R} \quad (1-21)$$

Next H_{app} is plotted against v_c and a curve fitting technique is used to extract the value of H_{app} at $v_c = 0$. Since 0 approach speed corresponds to the theoretically perfect static case, this will yield the true Hamaker constant.

$$H = H_{app}(v_c = 0) \quad (1-22)$$

The main limitations of this method is the time and computation effort it takes to perform the calculations. For this method to be used, a very similar process must be done to ensure H is calculated at a theoretical 0 sampling resolution. Another difficulty of this method is accurately measuring the tip radius R for use in equation 1-21. However, other authors have improved upon this method by using a calibration surface to get an effective tip radius R_e , hence avoiding the need for precise knowledge of tip geometry altogether [28].

1-8 Measuring the tip radius

The tip radius of the cantilever R can be measured in many different ways that don't involve imaging using a Scanning Electron Microscope (SEM) [31]. Many of these methods exploit the electrostatic forces that exists between the tip and sample because they are largely dependant on the geometry of the cantilever tip [32]. Two existing methods for extracting R using electrostatic forces have been outlined below.

1-8-1 Force vs static gap

The tip radius can be extracted from a force distance curve by fitting it to an analytical approximation of the electrostatic force [33]. The analytical approximation of the Electrostatic force can be modelled using a very simplified Generalized Image-Charge Method (GICM) [34], which resembles a flat plate capacitor model.

By applying a large DC tip voltage, the electrostatic force can be magnified allowing a fit to be extracted more reliably from the slope of the F_{ts} vs $1/z$ curve.

This method is very simple and effective at low static gaps. However, the simplified analytical model doesn't fully account for the capacitance gradient influences from the cone or cantilever base. Likewise, the method uses static AFM which can result in earlier snap-in at z values, limiting the most valuable data close to the sample.

1-8-2 DC voltage vs static gap

Another method uses dAFM under the influence of electrostatic forces to extract R [35]. In this method, an AC and DC tip voltage is applied to generate an electrostatic force with multiple frequency components. The DC tip voltage V_{DC} is varied while recording the static gap z as its regulated to give a constant force gradient. The force gradient is kept constant by controlling the resonance frequency of the cantilever to be constant. The corresponding $z - V_{DC}$ curve can be fitted to a simplified analytical model of the force gradient to extract R .

$$\begin{aligned} F_{elec} &= -\frac{\pi\epsilon_0 R(\Delta V)^2}{d} \\ F'_{elec} &= \frac{\pi\epsilon_0 R(\Delta V)^2}{d^2} \end{aligned} \quad (1-23)$$

Where ϵ_0 is the absolute permittivity constant and ΔV is the difference in voltage between the sample and the tip. F'_{elec} is the derivative of the electrostatic force F_{elec} with respect to d .

This method is effective because the $z - V_{DC}$ curve can also provide insights into the approximate shape of the cantilever tip. An additional advantage of this method is that it operates in FM-mode which is especially sensitive to the geometry of the tip apex due to the detection of the force gradient [36].

1-9 Conclusion

A summary of AFM operation and a brief review of existing methods to extract H and R has been presented. The literature indicates that it is possible to extract H by analyzing the motion of the tip in the presence of the VdW force. The literature also indicates that it is possible to extract R using electrostatic forces.

The trademark softening behavior that is expected to be observed when oscillating sufficiently close to the sample will be determined in part by the VdW force. Consequently, by carefully obtaining forward and backward frequency sweeps, H can be fitted and extracted. A difficulty in this method involves mitigating or modelling other adhesive

forces that could also produce softening behavior. Fortunately, a bias voltage can mitigate the electrostatic forces, and a hydrophobic sample in low humidity can minimize capillary forces.

Exploiting electrostatic forces are an ideal way to extract the tip radius because they are highly dependant on the geometry of the cantilever. The capacitance gradient is dominant at low static gaps, implying the tip radius can be extracted from capacitance gradient data generated using a simplified KPFM technique.

Chapter 2

Hamaker constant determination using Frequency Response Curves in Atomic Force Microscopy

Hamaker constant determination using Frequency Response Curves in Atomic Force Microscopy

M. James^a

^a*Precision and Microsystems Engineering, TU Delft, Delft, The Netherlands*

ARTICLE INFO

Keywords:

Atomic force microscopy
Hamaker constant
Frequency Response Curve
Van der Waals Force

ABSTRACT

A new method to extract the Hamaker constant using dynamic Atomic Force Microscopy (dAFM) is proposed. The Hamaker constant is extracted by fitting nonlinear Frequency Response Curves (FRCs) to analytical approximations of the amplitude and phase. A fast and robust optimization scheme is implemented to output the Hamaker constant, effective quality factor, and effective point force excitation. This method is validated by applying the fitting scheme to numerical data based on a point force excitation model. Two sets of formulas have been derived using the method of averaging. These formulas are analyzed statistically to provide an upper limit on the expected uncertainty in measuring the Hamaker constant.

1. Introduction

Atomic Force Microscopy (AFM) is a tool that has been traditionally used to image surfaces with nanometer resolution. In addition to imaging, AFM can be used to characterize materials at the nanoscale level. This is done by exploiting the large nonlinear tip-sample forces that exist between a microcantilever tip and sample. In nanotechnology, one of the challenges is to characterize the nanoscale interaction. In this framework, a key parameter is the Hamaker constant H . This constant is a measure of the strength of the Van der Waals (VdW) force [1], and varies depending on the material that makes up the tip and sample, and the surrounding medium [2]. The VdW force typically only interacts with the cantilever tip within a few nanometers or less [3, 4]. This makes H difficult for extraction largely because of the presence of other tip sample interaction forces. These can include but are not limited to electrostatic forces and capillary forces [5]. Additionally, when the cantilever tip approaches these small distances slowly, it is prone to snap-in - a phenomena in which the restoring force of the cantilever is overpowered by the net adhesive forces between the tip and sample.

This snap-in behavior can be exploited to measure H by recording the corresponding static gap jump [6]. However, this method is limited by the inherent assumptions behind static mode AFM. Since the substrate and the cantilever must realistically approach each other with a non zero approach speed, the cantilever system is inherently dynamic. Other methods improve upon this by using a ‘quasi-dynamic’ method [7]. In this case, the dynamics of snap-in are modelled into the equation for predicting H . However, this method is timely and requires high resolution static displacement curves.

The difficulties associated with snap-in can be mitigated by vibrating the cantilever base mechanically using a shaker piezo. In this case, the inertial forces that exist during an oscillation allow the tip to probe closer to the surface while minimizing the chance of snap-in. This method of dynamic

AFM (dAFM) has many additional advantages associated with it. One such advantage is that the amplitude and phase of the cantilever can contain information about the nonlinear interaction forces. A Frequency Response Curve (FRC) measures the steady state amplitude of the cantilever while the excitation frequency is gradually increased or decreased. If the cantilever tip is oscillating close to the sample in the attractive regime then the FRC will exhibit softening behavior. If the tip is oscillating purely in the attractive regime, and if these adhesive forces are sufficiently large to cause pronounced softening behavior, two unstable saddle node bifurcations can occur. One of these bifurcations occur at a low amplitude, whereas the other bifurcation will occur at a higher amplitude. Experimentally, a forward/backward frequency sweep results in a rapid increase/decrease in steady state amplitude. As a result, this creates an unstable amplitude branch in the FRC, leading to hysteresis.

The FRC is an ideal way to measure H . This is because the softening behavior caused by the VdW force can be fitted to an analytical model. Additionally, if the softening is sufficiently large such that hysteresis occurs, the peak of the FRC can be easily identified which can help facilitate a fitting.

Analytical equations for both amplitude and phase have been derived using the method of averaging. These equations have been fitted to numerical and experimental data to extract H and two other parameters: the effective excitation force F_0 , and the effective quality factor Q . To accomplish this fitting a robust optimization algorithm based on a modified least squares technique was implemented. A statistical analysis was also conducted which provides insight on the upper limit of uncertainty in the extracted H from an experimentally generated FRC. Lastly, a comparison between FRCs based on different models of the VdW force are discussed quantitatively.

This paper will have the following structure. First, in section 2, the analytical formulas for amplitude and phase is presented and discussed. In subsection 2.1, the optimization algorithm which can extract H and other parameters from FRC data is outlined. In section 4 the analytical expressions

ORCID(s):

based on different VdW force models are compared. In section 5, an upper limit in the uncertainty in H is discussed quantitatively. Lastly, an experimental FRC fitting has been discussed in section 6.

2. Hamaker constant using FRCs

Analytical approximations of the FRC by means of the method of averaging has been presented in the literature [8]. Using this method, equations for both the amplitude and phase have been derived. These equations assume that the tip oscillates exclusively in the presence of the VdW force, and that the point force harmonic excitation model is valid. Derivations for these equations have been outlined in section A-1 of appendix A.

$$\Omega = 1 \pm \frac{1}{2} \sqrt{\left(\frac{F_0}{kzr}\right)^2 - \left(\frac{1}{Q}\right)^2 - Hf(r, R, k, z)} \quad (1)$$

$$\Omega = 1 + \frac{1}{2Q \tan \alpha} - Hg(\alpha, R, k, z, F_0, Q) \quad (2)$$

Equation 1 captures the nondimensionalized excitation frequency $\Omega = \frac{\omega}{\omega_0}$ as a function of nondimensionalized amplitude $r = \frac{A}{z}$, and equation 2 captures the nondimensionalized excitation frequency as a function of phase α . Where ω is the piezo excitation frequency, ω_0 is the first natural frequency far from the sample, A is the amplitude, z is the static gap between tip and sample, F_0 is the excitation force, k is the stiffness, Q is the quality factor, H is the Hamaker constant, and R is the tip radius. The nonlinear components that describe the softening behavior of the FRC are $f(r, R, k, z)$ and $g(\alpha, R, k, z, F_0, Q)$. These terms depend on the VdW force model used. The general expression for the VdW force between a sphere (the cantilever tip) and a plane (the sample) is given by the following equation. [2, 9].

$$F_{VdW,1} = -\frac{2HR^3}{3d^2(2R+d)^2} \quad (3)$$

where d is the instantaneous tip sample separation. If the tip and sample are sufficiently close such that $R \gg d$, then the VdW force can be simplified to the following equation.

$$F_{VdW,2} = -\frac{HR}{6d^2} \quad (4)$$

The nonlinear frequency terms that correspond to the general VdW force model from equation 3 are denoted as $f_1(r, R, k, z)$ and $g_1(\alpha, R, k, z, F_0, Q)$. The nonlinear terms that correspond to the simplified VdW force model from equation 4 are denoted as $f_2(r, R, k, z)$ and $g_2(\alpha, R, k, z, F_0, Q)$ correspond to $F_{VdW,2}$. These terms have been outlined below.

$$f_1 = \frac{1}{6kr^2z^3} \left[\frac{(1-r^2)z^4 + 8R^3z + 12R^2z^2 + (6-r^2)Rz^3}{(4R^2 + 4Rz + (1-r^2)z^2)^{3/2}} + \frac{r^2(R+z) - z}{(1-r^2)^{3/2}} \right] \quad (5)$$

$$g_1 = \frac{k^2}{6F_0^2Q^2 \sin^2 \alpha} \left[\frac{F_0^2Q^2(R+z) \sin^2 \alpha - k^2z^3}{(k^2z^2 - F_0^2Q^2 \sin^2 \alpha)^{3/2}} + \frac{F_0^2Q^2(R+z) \cos^2 \alpha - F_0^2Q^2(R+z) + k^2(2R+z)^3}{(F_0^2Q^2 \cos^2 \alpha - F_0^2Q^2 + k^2(2R+z)^2)^{3/2}} \right] \quad (6)$$

$$f_2 = \frac{R}{6kz^3(1-r^2)^{3/2}} \quad (7)$$

$$g_2 = \frac{Rk^2}{6(k^2z^2 - F_0^2Q^2 \sin^2 \alpha)^{3/2}} \quad (8)$$

A comparison between these formulas will be presented in section 4. Equation 1 demonstrates that the natural frequency ω_n will decrease with increasing amplitude. The backbone curve, which is the locus of the natural frequency $\Omega_{bb} = \frac{\omega_n}{\omega_0}$, is given by the following equation.

$$\Omega_{bb} = 1 - Hf(r, R, k, z) \quad (9)$$

Equation 1 and equation 2 do not model in the repulsive force, these formulas are only valid for instantaneous tip sample gaps greater than the inter molecular distance a_0 . Hence these formulas are only valid within the amplitude range

$$0 \leq r \leq r_{peak} \leq 1 - \frac{a_0}{z} \quad (10)$$

Where $r_{peak} = \frac{F_0Q}{kz}$ is the maximum amplitude of the FRC. This value, and its corresponding frequency $\Omega_{peak} = 1 - Hf(r_{peak}, R, k, z)$ very accurately approximate the softening peak of the amplitude FRC. Likewise, it can be derived that $r = r_{peak} \sin \alpha$, which implies that the corresponding phase will occur approximately when $\alpha = \alpha_{peak} = \frac{\pi}{2}$. Lastly, it can also be shown that with sufficient softening behavior present, two unstable saddle node bifurcations can occur. As shown in figure 1, one bifurcation will occur approximately near the peak of the FRC. This is where a sudden decrease in steady state amplitude will be observed experimentally during a backwards frequency sweep. The other bifurcation will occur at a lower amplitude, and higher frequency. This is where an increase in steady state amplitude will be observed experimentally during a forwards frequency. Exact locations of these bifurcations can be found by solving for $\frac{d\Omega}{dr} = \frac{d\Omega}{d\alpha} = 0$.

2.1. Nonlinear identification algorithm

2.1.1. Amplitude - frequency fit

In order to identify H , a nonlinear identification algorithm has been developed using a least squares fitting technique. Amplitude and phase data were fitted to equations 1 and 2 separately. The fit was designed to output three fitting parameters; H , F_0 and Q . The excitation force on the cantilever is unknown since the raw base excitation signal is measured in volts. Likewise, the calibrated value of Q far

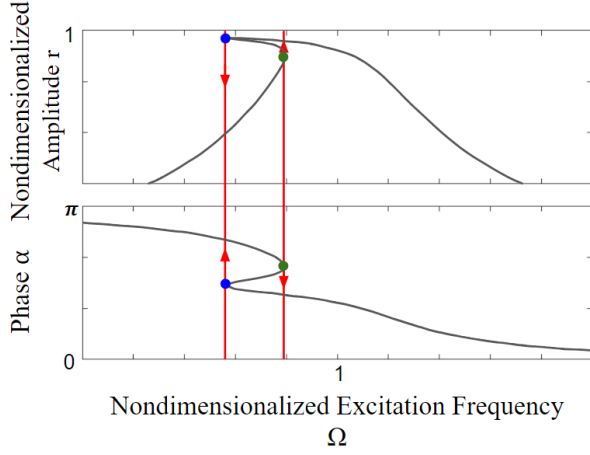


Figure 1: Plot showing softening due to the presence of the VdW force. Unstable saddle node bifurcations occur at the blue and green dots. A forward frequency sweep will result in an increase in amplitude and a decrease of phase. A backward frequency sweep will result in a decrease in amplitude and an increase in phase.

from the sample cannot be used due to the presence of nonlinear damping which is not modelled in analytical equations 1 and 2. Consequently, F_0 is an effective point force excitation term, and Q is an effective linear damping at a specific static gap.

The bi-stable response leads to more than one amplitude point per frequency. Consequently, traditional least squares fitting methods are inadequate to fit the amplitude FRC. In order to overcome this issue, a modified least squares fitting approach was utilized where the nonlinear curve and data were both sheared by an amount defined by the nonlinear function $Hf(r, R, k, z)$ from equation 1. This shearing causes the curve to become linear, facilitating a least squares fitting. Each non dimensionalized frequency and amplitude data point (Ω_i, r_i) was sheared horizontally by an amount $Hf(r_i, R, k, z)$.

$$\left(\Omega_{s,i}, r_{s,i}\right) = \left(\Omega_i + Hf(r_i, R, k, z), r_i\right) \quad (11)$$

$$r_s = \frac{F_0}{kz} \frac{1}{\sqrt{4\left(\Omega_s - 1\right)^2 + \left(\frac{1}{Q}\right)^2}} \quad (12)$$

The sheared data point is given in equation 11. The linear sheared curve is given by equation 12 and is derived in the section A-2 of appendix A. The subscript ‘s’ denotes the sheared data points or variables.

Equation 12 represents the new one-to-one sheared function, and equation 11 represents the new parameterised sheared data. A least squares technique can now be applied with the sheared function and sheared data. The optimization process involved minimizing the sum of the square of the vertical differences between each sheared data point and the sheared curve. This vertical difference is defined as L_i and is given by the following equation.

$$L_i = r_{s,i} - \frac{F_0}{kz} \frac{1}{\sqrt{4\left(\Omega_{s,i} - 1\right)^2 + \left(\frac{1}{Q}\right)^2}} \quad (13)$$

The fitting was desired to be most accurate near high amplitude regions of the FRC where softening behavior is observed. Consequently, a linear scaling was applied to each L_i^2 term whereby a larger weighting was applied to data points with larger amplitudes and a lower weighting was applied to data points with lower amplitudes.

$$S_i = cr_i \quad (14)$$

This scaling function S_i is given by formula 14 where c is a constant determining the strength of the linear scaling desired.

Multiple constraints were applied to the identification algorithm. Most of the constraints were linear and used to ensure that the parameter values rested in between a lower bound and upper bound of their expected value. The range of this lower and upper bound span several orders of magnitude for the parameters F_0 and H , whereas the range was made much smaller for Q to force the optimization not to deviate too strongly from the calibrated value of the quality factor Q_0 far from the sample. Two nonlinear equality constraints were also used to ensure that the peak of the FRC was always fitted. Thus, using amplitude FRC data to solve for the parameters F_0 , H , and Q , expressed in SI units, is equivalent to solving the following optimization problem.

$$\min \sum_{i=1}^N S_i \times L_i^2 \text{ such that } \begin{cases} 10^{-11} \leq F_0 \leq 10^{-4} \\ 10^{-22} \leq H \leq 10^{-15} \\ 0.4Q_0 \leq Q \leq 1.6Q_0 \\ r_{i,peak} = \frac{F_0 Q}{kz} \\ \Omega_{i,peak} = 1 - Hf\left(\frac{F_0 Q}{kz}, R, k, z\right) \end{cases} \quad (15)$$

Where $r_{i,peak}$ and $\Omega_{i,peak}$ is the unshered data point corresponding to the peak of a backwards frequency sweep data set. If the fitting procedure is applied to a forward frequency sweep data set, then the equality constraints need to be replaced with a broader nonlinear inequality constraint $r_{i,peak} < \frac{F_0 Q}{kz}$.

2.1.2. Phase - frequency fit

The phase - frequency fit was made using a more traditional horizontal least squares optimization. The fitting is similar to the amplitude - frequency fit explained in section 2.1.1, but with a few exceptions. Firstly, $L_i = \Omega_i - 1 - \frac{1}{2Q \tan \alpha_i} - Hg(\alpha_i, R, k, z, F_0, Q)$. Secondly, since in practice the phase of the base motion is typically not measurable, all the phase data can be offset by an unknown constant amount. Effectively, this means that there are 4 parameters to be found from the fit. F_0 , H , Q , and the offset. Using the formula $r = r_{peak} \sin \alpha$, the unstable saddle node during a backwards frequency sweep occurs approximately at $\alpha = \frac{\pi}{2}$. Hence an equality constraint to find the offset is

$$\text{offset} = \alpha_{i,peak} - \frac{\pi}{2} \quad (16)$$

Where $\alpha_{i,peak}$ is the phase data point corresponding to frequency $\Omega_{i,peak}$. If more accuracy is desired, this equality

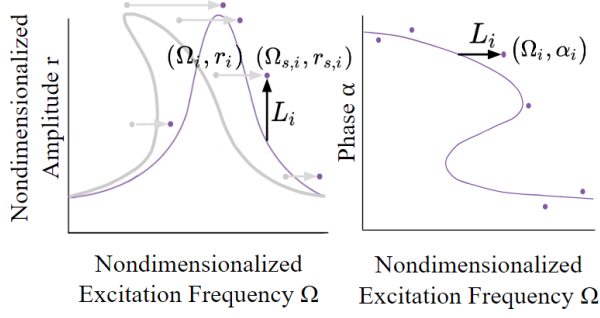


Figure 2: Amplitude and phase fitting scheme. A least Squares optimization was used to fit amplitude and phase data to analytical formulas 1 and 2. First the amplitude analytical equation and data are both sheared, and then the sheared amplitude data $(\Omega_{s,i}, r_{s,i})$ is fitted to the sheared function (equation 12). The unshered (raw) data and analytical formula fit is shown in grey. The phase fit uses a horizontal least squares method.

constraint can be made as an initial guess for the curve fitting algorithm instead. Lastly, an inequality constraint can be used to ensure that the curve is convex if the data shows the presence of an unstable saddle node bifurcation at $\alpha = \frac{\pi}{2}$. Thus using phase data to solve for parameters F_0 , H , Q and offset, expressed in SI units, is equivalent to solving the following optimization problem.

$$\min \sum_{i=1}^N L_i^2 \text{ such that } \begin{cases} 10^{-11} \leq F_0 \leq 10^{-4} \\ 10^{-22} \leq H \leq 10^{-15} \\ 0.4Q_0 \leq Q \leq 1.6Q_0 \\ \frac{d^2\Omega}{d\alpha^2} \Big|_{\alpha=\pi/2} > 0 \\ \Omega_{i,peak} = 1 - Hg\left(\frac{\pi}{2}, R, k, z, F_0, Q\right) \\ \text{offset} = \alpha_{i,peak} - \frac{\pi}{2} \end{cases} \quad (17)$$

3. Numerical FRC

Equations 1 and 2 were especially important to validate numerically because they were derived using a point force excitation model assuming small damping and VdW force.

The numerical FRCs were generated using the more accurate nondimensionalized base excitation model. In this equation $x = \frac{q}{z}$ is the non nondimensionalized displacement, $\tau = t\omega_0$ is the nondimensionalized time, and $\Omega = \frac{\omega}{\omega_0}$ is the non dimensionalized excitation frequency.

$$x'' + \frac{1}{Q}x' + x = \Omega^2 \frac{Y}{z} \sin(\Omega\tau) - \Omega \frac{Y}{z} \frac{1}{Q} \cos(\Omega\tau) + \frac{F_{ts}(z + zx + Y \sin \Omega\tau)}{zk} \quad (18)$$

Where Y is the amplitude of base motion, z is the static gap, Q is the quality factor, q is the displacement of the tip from static equilibrium, and t is time. Where $F_{ts}(d) = F_{VdW,1}(d) = -\frac{2HR^3}{2d^2(2R+d)^2}$ is the tip sample interaction force which is assumed just to consist of the general VdW force.

The base excitation formula features sin and cos excitation terms which can be combined to produce a small forcing phase offset $\alpha_{force} = \tan^{-1}\left(\frac{1}{\Omega Q}\right)$.

Figures 3a - 3d show amplitude and phase FRCs being fitted. Many more numerical experiments are outlined in section A-3 of appendix A. Each numerical data set consists of 3 FRCs generated at different nondimensionalized base excitation amplitudes Y/z . This numerical data was fitted by the analytical formulas using the inbuilt `fmincon` function in MATLAB with objective function and constraints described in section 2.1. The fits outputted the parameters F_0 , H and Q . The quality factor Q was extracted very accurately because the phase and amplitude far from resonance show negligible nonlinearities. The effective point force excitation very closely aligns with the formula $\frac{F_0}{kz} \approx \frac{Y}{z}$, as expected for experiments around resonance $\Omega^2 \frac{Y}{z} \sin(\Omega\tau) \approx \frac{Y}{z} \sin(\Omega\tau)$, with low damping $\Omega \frac{Y}{z} \frac{1}{Q} \cos(\Omega\tau) \approx 0$. H is the hardest parameter to extract because of its extremely high sensitivity. The experiment as shown in figure 3a - 3d managed to fit H with an average relative error of 5% for the amplitude FRCs and 12% for the phase FRCs. The error is quite small in this case largely because the static gap is low enough to create very pronounced softening behavior. In practice, the amplitude FRC is expected to extract H more accurately because the phase offset will need to be an additional fitting parameter as discussed in section 2.1.2.

Even unrealistically large VdW forces with low Q can be fitted surprisingly well. The numerical experiment shown in figure A-4 of section A-3 of appendix A was generated with $H = 4000 \times 10^{-19}\text{J}$, which undermines the small nonlinearities assumption behind method of averaging. Likewise, a low quality factor $Q = 60$ exaggerates the difference between the point force excitation model and the base excitation model. Despite this, H is predicted quite accurately, indicating the robustness of this method. This is also in line with the existing literature that the point force excitation model adequately approximates the base excitation model for $Q > 100$ [10]. This also shows that experiments which feature unfittable features are likely due to the presence of additional nonlinear tip sample forces.

4. Comparison between analytical Formulas

A quantitative comparison between the two amplitude FRC's presented in equation 1 was undertaken. Specifically, the difference between the FRC corresponding to the general VdW force expression ($f = f_1$) and the FRC corresponding to the simplified VdW force expression ($f = f_2$) was analyzed.

The difference between the curves was defined by the differences between peaks of both FRC's. Since both curves will share the same maximum amplitude $r_{peak} = \frac{F_0 Q}{kz}$, the difference was thus measured as the nondimensionalized excitation frequency difference between the peaks:

$$|\Delta\Omega_{peak}| = |Hf_1(r_{peak}, R, k, z) - Hf_2(r_{peak}, R, k, z)| \quad (19)$$

Hamaker Constant Using Frequency Response Curves

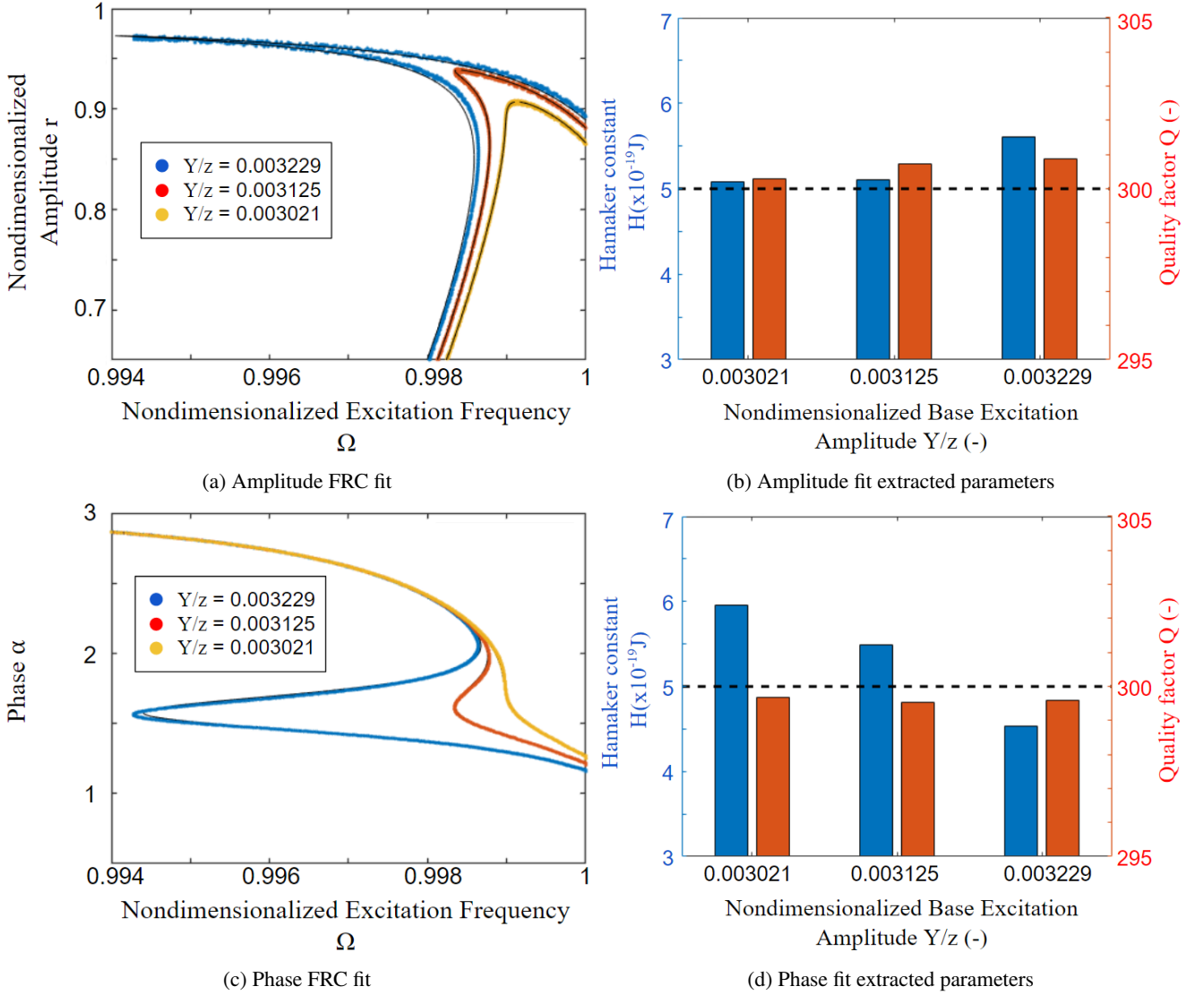


Figure 3: Fitting 3 numerical FRC data sets (blue/red/yellow) to analytical formulas (black) 1 and 2 (with $f = f_1$ and $g = g_1$). The numerical data was generated using a base excitation model with uniformly distributed noise added ($A/z_{noise} = 0.002$). Figures 3b and 3d show the extracted parameters from the fits. The effective F_0 extracted for amplitude were 1.45nN, 1.5nN, 1.56nN, and for phase were 1.43nN, 1.5nN, 1.56nN. Values used to generate numerical data, which are also shown by the black dotted line are $k = 24\text{N/m}$, $z = 20\text{nm}$, $R = 150\text{nm}$, $H = 5 \times 10^{-19}\text{J}$, $Q = 300$.

A worst case scenario was analyzed for comparing the FRCs. This was done by using an excitation force such that the curves were both on the verge of exhibiting a hardening type nonlinearity. $F_0 = \frac{kz}{Q}(1 - \frac{a_0}{z})$.

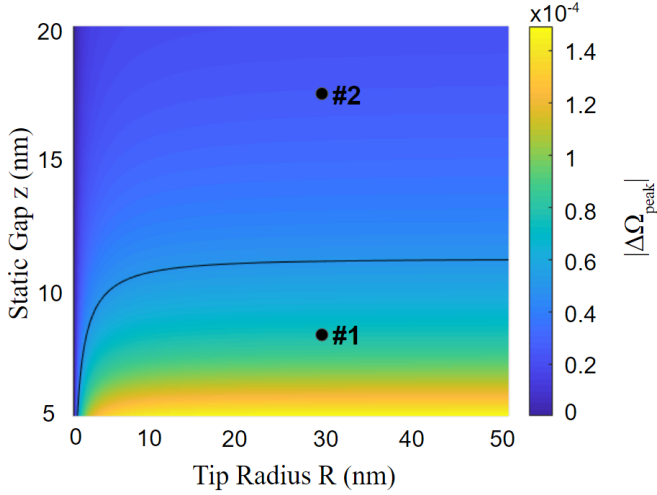
Figure 4a shows how tip radius and static gap influence the difference between the analytical formulas. The tip radius has a negligible effect except for extremely sharp tips. This is because the VdW force is extremely small for small values of R . The static gap has a much larger influence, especially for low values of z . Thus for a typical cantilever, if imaging close to the surface (<10nm) it's necessary to account for the more general VdW force when producing Frequency Response Curves.

5. Error Propagation

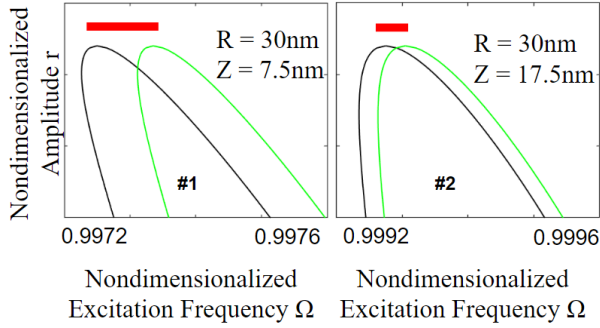
A statistical analysis of formula 1 was undertaken to find the error propagated to the Hamaker constant ΔH due to uncertainty in three calibrated parameters; stiffness Δk , natural frequency $\Delta\omega_0$, and static gap Δz . The formula to predict error propagation is provided below.

$$\Delta H = \sqrt{\left(\frac{\partial H}{\partial k} \Delta k\right)^2 + \left(\frac{\partial H}{\partial \omega_0} \Delta \omega_0\right)^2 + \left(\frac{\partial H}{\partial z} \Delta z\right)^2} \quad (20)$$

Since a fitting was done to the whole FRC, the value of amplitude used when evaluating the partial derivatives was the value corresponding to the minimum ΔH . Also, the uncertainties $\Delta k = 0.064 \text{ N/m}$, $\Delta\omega_0 = 1.85 \text{ Hz}$ were calculated with a 95% confidence based on 12 calibrations using the hydrodynamic function method with a ElectriTap150-G cantilever. The uncertainty in quality factor $\Delta Q = 3.26$, but



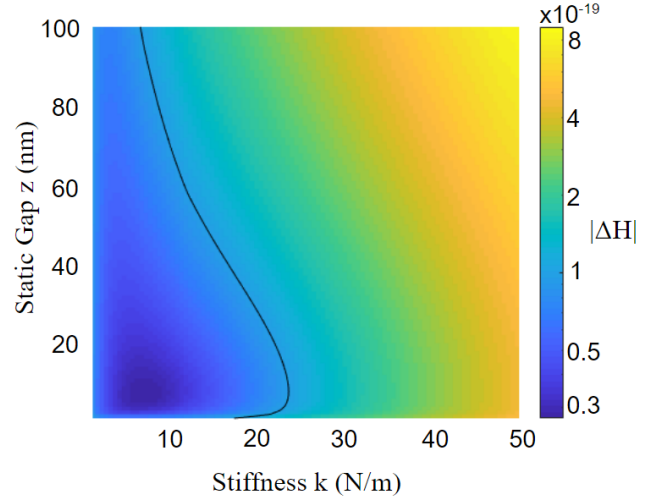
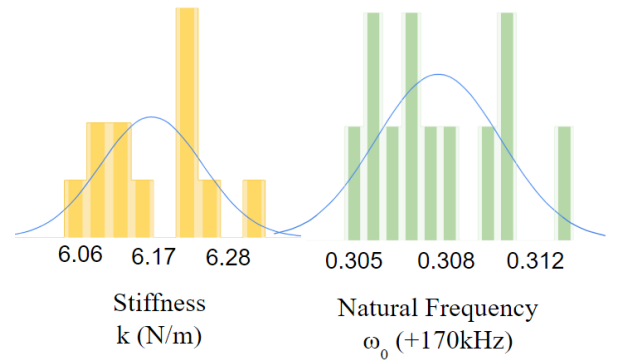
(a) Difference between analytical formulas map



(b) Points on map

Figure 4: Color plot showing the difference between the amplitude FRC's when using different VdW force models. Figure 4b shows the difference between the formulas at two different tip radius and static gap values. The green FRC corresponds to the response when the generalized VdW force model is used ($f = f_1$) and the black FRC corresponds to equation when the simplified VdW force model is used ($f = f_2$). $|\Delta\Omega_{peak}|$ is the nondimensionalized excitation frequency difference between the peaks of the two FRC curves, and is indicated by a thick red line. The black curve shows a isoline corresponding to $|\Delta\Omega_{peak}| = 5 \times 10^{-5}$. Hence, combinations of parameters (z, R) above this line correspond to a negligible difference between FRC's, whereas combinations below this line correspond to a significant difference. $k = 23.1\text{N/m}$, $H = 4 \times 10^{-19}\text{J}$, $Q = 377$, $a_0 = 0.7\text{nm}$.

was not included in the error propagation formula since Q was a fitting parameter. A conservative estimate of $\Delta z = 0.2\text{nm}$ was chosen, and the uncertainty in amplitude and frequency were assumed to be 0 such that a 'best case' error propagation analysis could be undertaken. Likewise F_0 was chosen to correspond to when the FRC is at the onset of hardening $F_0 = \frac{kz}{Q}(1 - \frac{a_0}{z})$. As can be seen in figure 5a it's desirable to measure FRC's at low static gaps with low stiffness cantilevers. However, in practice z needs to be large enough such that snap-in doesn't occur during measurements. Hence, even in the most ideal experiment where a cantilever has a stiffness of $k \approx 7\text{N/m}$ and a static gap of $z \approx 7\text{nm}$, the error in the Hamaker constant is expected to


 (a) Error propagated to H


(b) Normal Distributions

Figure 5: Figure 5a is a color plot showing error propagated to H due to uncertainty in stiffness $\Delta k = 0.064\text{N/m}$, natural frequency $\Delta\omega_0 = 1.85\text{Hz}$ and static gap $\Delta z = 0.2\text{nm}$. The black isoline corresponds to $\Delta H = 1 \times 10^{-19}\text{J}$. The minimum error propagated occurs at $z = 7\text{nm}$ and $k = 7\text{N/m}$ and is $\Delta H_{min} = 2.71 \times 10^{-20}\text{J}$. The values chosen were $Q = 300$, $H = 4 \times 10^{-19}\text{J}$, $a_0 = 0.7\text{nm}$ and $R = 60\text{nm}$. Figure 5b shows bell curves generated from 12 calibrations. The middle number is the mean, and the outer numbers correspond to one standard deviation from the mean.

be in the order of $\Delta H \approx 10^{-20}$ or higher.

6. Experimental Investigation

Experimental FRC's were generated using a setup consisting of a commercially available Nanosurf FLEX AFM, and an external Multi-frequency Lock-In Amplifier (MLA) from Intermodulation Products. A C3000 controller was also used to position the base of the cantilever for each experiment. The experiment was conducted in air at 24°C with an ElectriTap150 cantilever with Platinum overall coating. The sample was freshly cleaved Highly Oriented Pyrolytic Graphite (HOPG). The experiment was also under an acoustic hood, and inside a humidity chamber with a relative humidity reading of 7%RH. The tip radius $R = 20\text{nm}$ was measured from a SEM image, and the stiffness $k = 6.54\text{N/m}$,

Hamaker Constant Using Frequency Response Curves

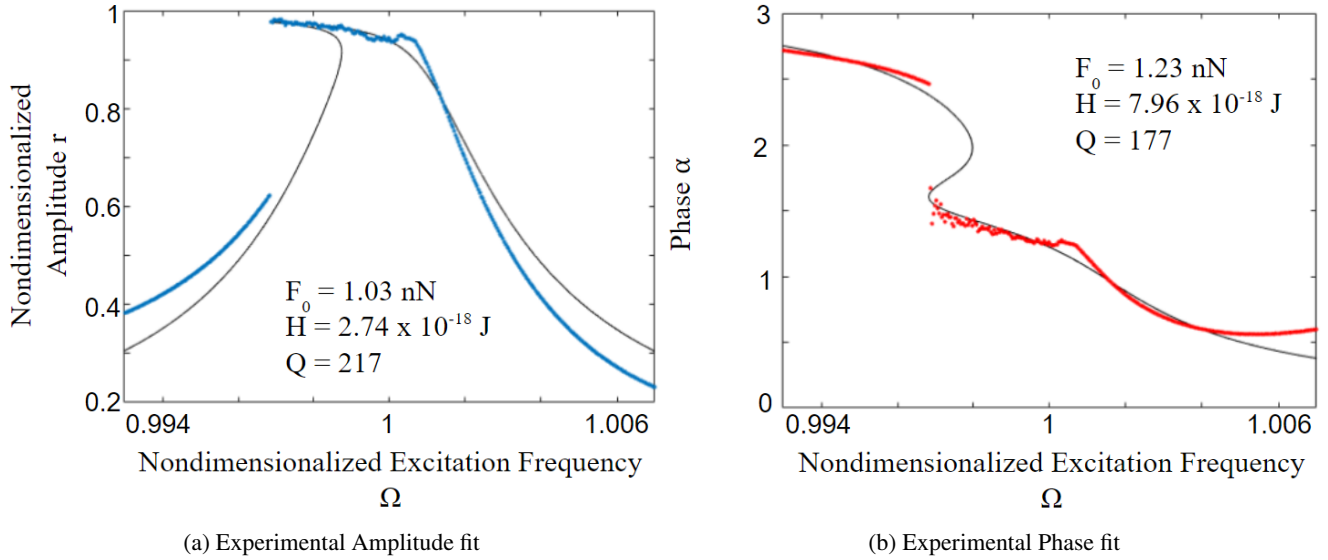


Figure 6: Experimental backwards frequency sweep data fitted with the analytical formula from equation 1 (with $f = f_1$) and equation 2 (with $g = g_1$). The amplitude and phase data are colored blue and red respectively, and the black curves are the analytical formula fits. F_0 , H and Q are the parameters extracted from each fit. The experiment was done with a ElectriTap150 cantilever with overall platinum coating on a HOPG sample at $z = 35\text{nm}$. The calibrated parameters far from the sample were $k = 6.54\text{N/m}$, $Q = 332.4$, $\omega_0 = 170.297\text{kHz}$. $R = 20\text{nm}$.

quality factor $Q = 332.4$, and natural frequency $\omega_0 = 170.297\text{kHz}$ were measured using the hydrodynamic function method using the MLIA. The MLIA calibration also recorded a sensitivity of 514.36nm/V .

The experimental amplitude and phase curves shown in figure 6a and 6b were generated from a backwards frequency sweep.

As can be seen in figure 6a, the maximum non dimensionalized amplitude is slightly less than 1, which is expected since the VdW force typically has a range of a few nanometers [11, 4]. The sides of the amplitude FRC are poorly aligned likely for three main reasons. Firstly, the natural frequency far from the sample ω_0 could have decreased once in contact with the surface prior to the FRC. This is a possibility since the tip could have picked up some additional water mass upon contact. Also, additional influences of other modes at higher resonances (which aren't modelled) could also have adjusted the amplitude data. Additionally, amplitude dependant damping is likely present which can't be fully captured by a linearized effective Q . Base excitation is unlikely a cause since numerical experiments simulated under the base excitation model with high damping (low Q) align very well with the analytical equations 1 and 2.

As can be seen in figure 6b, the phase is fitted quite well, especially around the unstable saddle node bifurcation at $\alpha = \frac{\pi}{2}$. However, at larger frequencies the phase unexpectedly flicks upwards. This is likely due to a frequency dependant phase offset caused by the piezo or other equipment that can't be modelled.

The Hamaker constant extracted from both the amplitude and phase data is extremely large. This can be explained in part because long range electrostatic forces that exist between the tip and sample were not nullified with a bias volt-

age in this experiment. Also, the static gap used in this experiment is approximate since the static displacement set-point of 2nm was also neglected. Accounting for this set-point causes the peak nondimensionalized amplitude to be greater than 1.

Multiple other FRCs were also produced at different static gaps in which softening behavior was also observed. However, these other experiments showed a nondimensionalized amplitude larger than 1 - which is impossible in reality since it corresponds to the cantilever penetrating into the sample during an oscillation and still feeling a purely attractive force. These additional experiments are shown and discussed in section A-4 of appendix A. A few experimental problems can help explain this phenomena. Firstly, the sensitivity value recorded by the MLA is likely a large source of error, and can be exasperated due to a slight misalignment of the laser on the tip of the cantilever. Secondly, z -fluctuation of around $0.5\text{-}2\text{nm}$ was observed, which is significant considering the short range nature of the VdW force. These z -fluctuations are speculated to be caused by piezo creep and thermal fluctuations. Thirdly, $x - y$ variation of the cantilever above the surface could expose the tip to slightly different forces for each set of experiments. Lastly, the high reflectivity of the surface could interfere with the deflection measurement from the 4 quadrant photo diode at very low static gaps.

Further explanation of the nature of the technical issues, potential solutions, and additional corresponding experiments is discussed in sections A-5 and A-6 of appendix A.

Lastly, the HOPG sample used in the experiment shown in figure 6 is hydrophobic. Non hydrophobic samples at humidities greater than $5\%RH$ are likely to affect the the reliability of FRCs due to the presence of strong capillary forces. This is elaborated on in section A-7 of appendix A.

7. Conclusion

A method to extract the Hamaker constant using analytical approximations for nonlinear frequency response curves has been proposed. Many experimental FRCs were generated and fitted. However, the extracted H was unreliable in these experiments due to technical limitations which have been discussed. Despite being unable to validate this experimentally, numerical experiments with added artificial noise indicate that H can be measured using a robust identification algorithm. However, a theoretical upper limit of uncertainty in the extracted H is approximately 3×10^{-20} J. Experiments aiming to extract H accurately should do so with soft cantilevers at low static gaps, and account for the general VdWs force.

References

- [1] Ronald G Reifenger. *Fundamentals of Atomic Force Microscopy: Part I: Foundations*. World Scientific Publishing Company Pte Limited, 2016.
- [2] Riccardo Borgani, Daniel Forchheimer, Jonas Bergqvist, Per-Anders Thorsell, Olle Inganäs, and David B Intermodulation electrostatic force microscopy for imaging surface photo-voltage. 105(14):143113, 2014.
- [3] Hans-Jürgen Butt. Measuring electrostatic, van der waals, and hydration forces in electrolyte solutions with an atomic force microscope. *Biophysical Journal*, 60(6):1438–1444, 1991.
- [4] Daniel Forchheimer, Daniel Platz, Erik A Thorsell, and David B Haviland. Simultaneous imaging of surface and magnetic forces. *Applied Physics Letters*, 103(1):013114, 2013.
- [5] Lothar Zitzler, Stephan Herminghaus, and Frieder Mugele. Capillary forces in tapping mode atomic force microscopy. *Physical Review B*, 66(15):155436, 2002.
- [6] B Gady, D Schlee, R Reifenger, and DS Rimai. The interaction between micrometer-size particles and flat substrates: A quantitative study of jump-to-contact. *The Journal of Adhesion*, 67(1-4):291–305, 1998.
- [7] Sean G Fronczak, Jiannan Dong, Christopher A Browne, Elizabeth C Krennek, Elias I Franses, Stephen P Beaudoin, and David S Corti. A new “quasi-dynamic” method for determining the hamaker constant of solids using an atomic force microscope. *Langmuir*, 33(3):714–725, 2017.
- [8] Shuiqing Hu and Arvind. Analytical formulas and scaling laws for peak interaction forces in dynamic atomic force microscopy. 91(12):123106, 2007.
- [9] C Argento and RH. Parametric tip model and force-distance relation for hamaker constant determination from atomic force microscopy. 80(11):6081–6090, 1996.
- [10] Tomás R Rodríguez and Ricardo. Tip motion in amplitude modulation (tapping-mode) atomic-force microscopy: Comparison between continuous and point-mass models. 80(9):1646–1648, 2002.
- [11] J. N. Munday. Measured long-range repulsive casimir forces. *Nature*, 457(7226):170, 2009.

Chapter 3

Tip radius determination using a simplified Kelvin Probe Force Microscopy technique

Tip radius determination using a simplified Kelvin Probe Force Microscopy technique

M. James^a

^aPrecision and Microsystems Engineering, TU Delft, Delft, The Netherlands

ARTICLE INFO

Keywords:

Atomic force microscopy
Tip radius
Kelvin probe force microscopy
Cantilever geometry
Electrostatic Forces

ABSTRACT

A new method to extract the tip radius using electrostatic forces is presented. The method uses a simplified Kelvin Probe Force Microscopy (KPFM) technique in which the cantilever is electrically excited at different static gaps. The capacitance gradient at each point is measured by sweeping the DC tip voltage and recording the corresponding amplitude. The following capacitance gradient vs static gap data set is fitted to an analytical model to extract the tip radius, cone angle and tip height.

1. Introduction

Kelvin Probe Force Microscopy (KPFM) is a non-contact variant of Atomic Force Microscopy (AFM) that can measure the surface potential (or surface voltage V_s) of a sample [1, 2]. One popular method of KPFM involves scanning the topography of a sample by exciting the cantilever mechanically via the piezo at the first natural frequency, and simultaneously measuring V_s by electrically exciting the cantilever tip (usually) at the second natural frequency. ‘Lift mode’ is another popular technique in which the cantilever makes two passes along each scan line. During the first pass the topography is measured by exciting the cantilever mechanically at its first resonance, and during the second pass V_s is measured by exciting the cantilever electrically at its first resonance [3]. In either case, when the tip is excited electrically it is done so by applying a voltage to the cantilever tip which consists of a DC component V_{DC} and an AC component $V_{AC} \sin(\omega_{elec}t)$. V_s is thus calculated by using a feedback loop which adjusts V_{DC} so that the component of the electrostatic force at ω_{elec} , $F_{\omega_{elec}}$, is minimized.

There are many advantages of applying KPFM that go beyond imaging the surface potential of a sample. Firstly, the electrostatic force that exists between the cantilever tip and a point on the surface can be measured and nullified by setting V_{DC} equal to V_s . This DC voltage is known as the bias voltage and can be visualized by observing the minimum of the V-shaped $F_{\omega_{elec}}$ vs V_{DC} curve [4]. It’s possible to extract the force component directly using an Electrostatic Force Microscopy Lock in Amplifier (EFM LIA). Another advantage of KPFM is the ability to extract information about the capacitance gradient $\frac{dC}{dz}$. For example, the capacitance gradient can be extracted by analyzing the motion at ω_{elec} [5], or it can be extracted by analyzing the motion of the cantilever at $2\omega_{elec}$. [6].

Fortunately, the tip radius R can be extracted using long range electrostatic forces [7] largely because the capacitance between the cantilever and sample is determined in part by the geometry of the cantilever tip [8, 9].

There have been many attempts to extract the tip radius using electrostatic forces. One method fits force-distance

data to a analytical expression derived using the Generalized Image-Charge Method (GICM) [10, 11]. Another method includes sweeping DC voltage and recording tip sample gap as the force gradient is controlled to be constant, and curve fitting this data to a capacitance gradient, $\frac{dC}{dz}$, model [12]. The tip radius can also be found by fitting cantilever deflection vs sample displacement to a model based on a another expression for $\frac{dC}{dz}$ [13]. All of these methods use a simple analytical approximation of the capacitance gradient that resembles a flat plate capacitor model. This model is only accurate extremely close to the sample where snap-in phenomena is observed. In this paper, a non contact simplified KPFM method is proposed which accounts for the capacitance gradient components of the tip apex and cone, allowing additional properties of the cantilever tip to be extracted. Section 2 will summarize the theory and assumptions used to extract the capacitance gradient and tip geometry. sections 3 and 4 present and analyze an experiment that validates this concept. Lastly, section 5 outlines the identification algorithm used to fit data.

2. Theory

The electrostatic force between the tip and sample in its most general form is

$$F_{elec} = -\frac{1}{2} \frac{dC}{dz} \Delta V^2 \quad (1)$$

Where ΔV is the difference between the surface voltage V_s and the tip voltage which consists of both a DC component V_{DC} and an AC component $V_{AC} \sin(\omega_{elec}t)$. [1]

$$\begin{aligned} F_{elec} &= -\frac{1}{2} \frac{dC}{dz} \left(V_s - V_{DC} - V_{AC} \sin(\omega_{elec}t) \right)^2 \\ &= -\frac{1}{2} \frac{dC}{dz} \left((V_s - V_{DC})^2 - 2(V_s - V_{DC})V_{AC} \sin(\omega_{elec}t) \right. \\ &\quad \left. + \frac{1}{2} V_{AC}^2 (1 - \cos(2\omega_{elec}t)) \right) \end{aligned} \quad (2)$$

The force can be split up into three separate components $F_{elec} = F_{elec0} + F_{elec1} + F_{elec2}$. Each force component has

ORCID(s):

contributions at different frequencies; 0, ω_{elec} and $2\omega_{elec}$.

$$\begin{aligned} F_{elec0} &= -\frac{1}{2} \frac{dC}{dz} \left((V_s - V_{DC})^2 + \frac{1}{2} V_{AC}^2 \right) \\ F_{elec1} &= \frac{dC}{dz} (V_s - V_{DC}) V_{AC} \sin(\omega_{elec} t) \\ F_{elec2} &= \frac{1}{4} \frac{dC}{dz} V_{AC}^2 \cos(2\omega_{elec} t) \end{aligned} \quad (3)$$

If the system is exposed to this force far from the sample such that there are no other tip sample interaction forces present, and if the static gap remains roughly constant, and if there is no external excitation from the piezo, then the equation of motion becomes linear.

$$\frac{1}{\omega_0^2} \ddot{q} + \frac{1}{Q\omega_0} \dot{q} + q = \frac{1}{k} F_{elec}(t) \quad (4)$$

Where q is the displacement of the tip from static equilibrium. Since the EoM is linear, the superposition theorem applies and each term can be solved for independently. The steady state amplitude corresponding to the forcing component $F_{elec1} = \frac{dC}{dz} (V_s - V_{DC}) V_{AC} \sin(\omega_{elec} t)$ yields equation 5. The $\frac{dC}{dz}$ term is assumed constant, which is a reasonable approximation if the amplitude of oscillation is much less than the static gap.

$$A = \left| \frac{\frac{dC}{dz} (V_{DC} - V_s) V_{AC}}{k} \times \frac{1}{\sqrt{(1 - (\frac{\omega_{elec}}{\omega_0})^2)^2 + (\frac{1}{Q} \frac{\omega_{elec}}{\omega_0})^2}} \right| \quad (5)$$

Since the other forcing terms are at distinct frequencies far from ω_{elec} they will not contribute largely to the amplitude at ω_{elec} . Hence, it is reasonable to assume a LIA at ω_{elec} should accurately measure A . Equation 5 can be simplified further if the AC voltage is set to oscillate at the first natural frequency of the system $\omega_{elec} = \omega_0$.

$$A = \left| \frac{\frac{dC}{dz} V_{AC} Q}{k} (V_{DC} - V_s) \right| \quad (6)$$

As can be seen in equation 6, exciting the system at the natural frequency will scale up the amplitude measured by the LIA, hence improving the signal-to-noise ratio. Also, since A is linear with V_{DC} , an experimental plot will yield a V-shaped curve. Simply observing the DC voltage which corresponds to the minimum amplitude will identify the bias voltage $V_{DC} = V_s$.

The magnitude of the slope of the A - V_{DC} curve provided in equation 6 is $\frac{dC}{dz} V_{AC} Q/k$. The magnitude of the AC voltage, V_{AC} , is a free parameter to choose for each curve, and k and Q can be measured in a separate thermal calibration. Hence the only unknown constant, $\frac{dC}{dz}$, can be found by measuring slope of each A - V_{DC} curve. Since the capacitance is largely a function of the geometry of the cantilever, this value of $\frac{dC}{dz}$ can be used to extract properties of the cantilever. The total capacitance, C , between the tip and sample is made up

from 3 distinct components; the tip apex, the the tip cone and the lever. In effect this means

$$\frac{dC}{dz} = \frac{dC}{dz_{apex}} + \frac{dC}{dz_{cone}} + \frac{dC}{dz_{lever}} \quad (7)$$

Full analytical approximations for each of these components have been recorded in the literature [7] and are written in appendix B. These formulas demonstrate that for medium with large tip sample gaps the $\frac{dC}{dz_{cone}}$ and $\frac{dC}{dz_{lever}}$ components dominate. This is an undesired situation since these terms are very weakly dependant on the tip radius, making curve fitting $\frac{dC}{dz}$ to find R difficult. However, for small tip sample gaps the $\frac{dC}{dz_{apex}}$ term dominates [8]. Thus, to perform a tip radius extraction, a Goldilocks region for z is needed; the cantilever needs to be close enough such that the $\frac{dC}{dz_{apex}}$ is pronounced, but it also needs to be far enough away such that presence of other forces are negligible.

The full capacitance gradient expression is an exhaustive but complete approach which was used for extracting R in the following experiments. However, the $\frac{dC}{dz}$ components can be simplified at small tip sample gaps z , allowing for a simpler fitting. Firstly, the cone and lever components of the capacitance gradient remain roughly constant at small z values.

$$\frac{dC}{dz_{cone}} + \frac{dC}{dz_{lever}} = \text{constant} \quad (8)$$

Additionally, the tip component $\frac{dC}{dz_{apex}}$ can be simplified at small static gaps z , and can be modelled as a sphere interacting with an infinite plane (the sample). In this case, the capacitance gradient can be given by equation below [8].

$$\frac{dC}{dz_{apex}} = -2\pi\epsilon \frac{R^2}{z^2 + Rz} \quad (9)$$

Where R is the tip radius, z is the static gap, and ϵ is the absolute permittivity constant.

3. Experiment

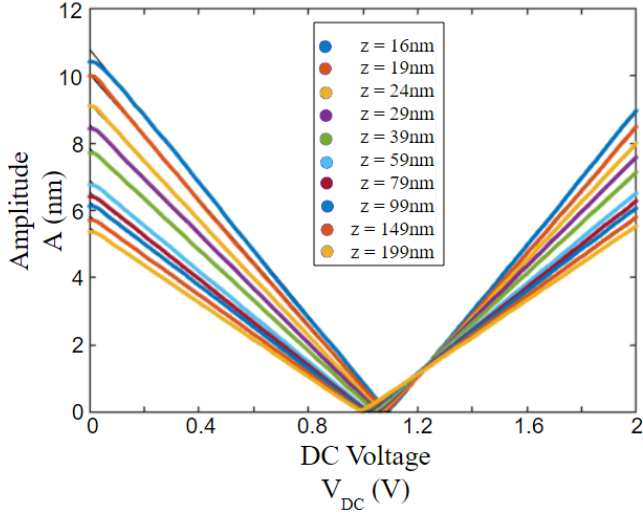
3.1. Experimental setup

A commercial AFM (Nanosurf FLEX operated with the C3000 controller) was used to position the cantilever at a set static gap z for each $A - V_{DC}$ curve. The AFM head was placed in a humidity chamber with an acoustic hood to minimize influence of capillary forces and noise.

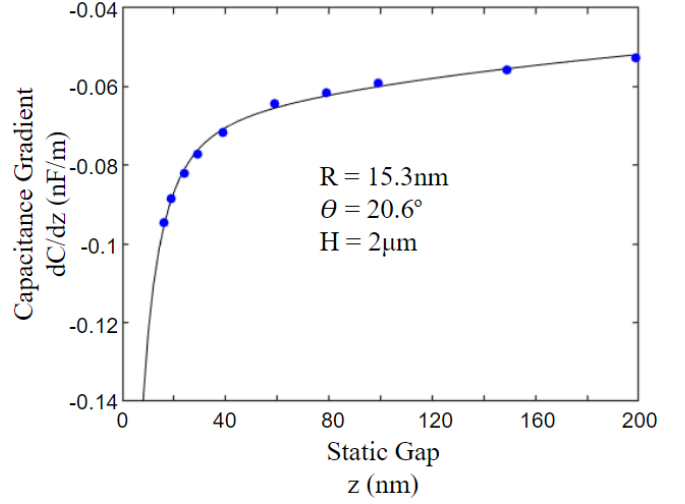
An experiment was done using an ElectriTap150-G cantilever on a freshly cleaved Highly Oriented Pyrolytic Graphite (HOPG) sample. The humidity measured in the chamber was 7% and the AC voltage chosen was $V_{AC} = 2V$. One set of SEM images was preformed before the experiment to validate the result.

Since both experiments were not conducted in vacuum, a dielectric constant at 20°C, 1 atm, and 10% humidity was used [14].

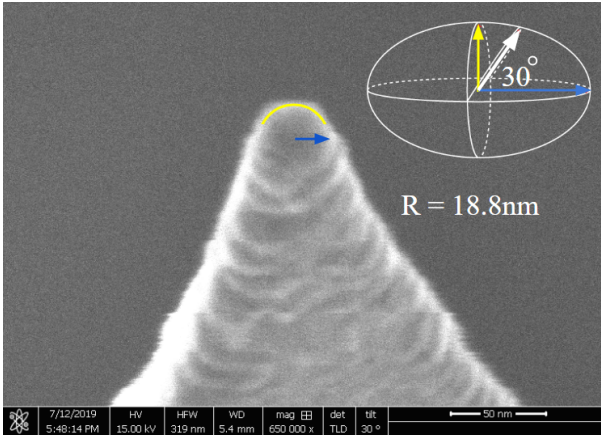
Extracting Tip Radius



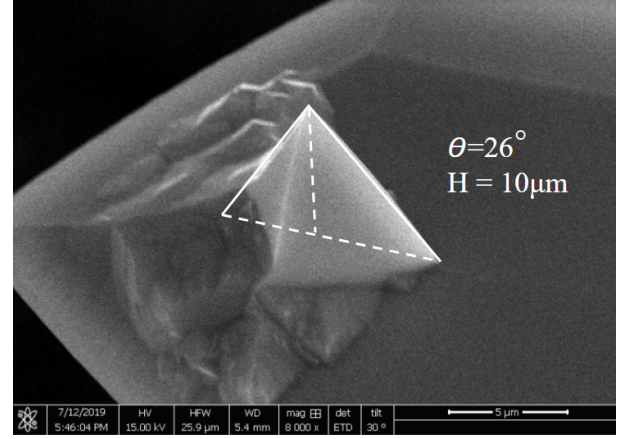
(a) $A-V_{DC}$ curves at discrete static gaps z



(b) Capacitance gradient curve



(c) ElectriTap150 cantilever tip apex



(d) ElectriTap150 cantilever tip zoomed out

Figure 1: ElectriTap150 cantilever with overall platinum coating with HOPG sample at 7% humidity and $V_{AC} = 2V$. Figure 1a shows multiple V-shaped $A - V_{DC}$ curves which were measured at discrete static gaps z in order to extract a profile of the bias voltage V_{bias} and capacitance gradient $\frac{dC}{dz}$. Figure 1b shows the extracted capacitance gradient data which was used to calculate the cantilever geometry by fitting it to an analytical model. The extracted tip radius was $R = 15.3nm$ which is in rough alignment with the SEM image of the cantilever tip from figure 1c which shows a tip radius of $R = 18.8nm$. Figure 1d shows a zoomed out view of the cantilever tip with significantly different values of cone angle and tip height. Both SEM images were made at a tilt of 30 degrees. Calibrated values were $Q = 288$ and $k = 5.52N/m$.

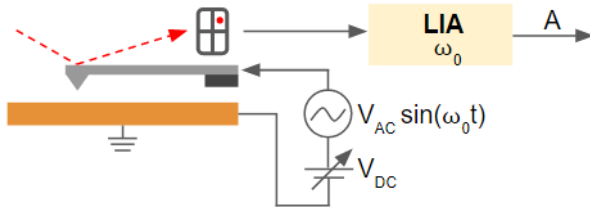


Figure 2: Schematic showing input AC and DC voltage being applied to the tip at the first natural frequency ω_0 , and output amplitude at the first natural frequency.

3.2. Method

A simplified KPFM technique was used to extract the tip radius R . The method involves the following 5 steps:

1. Excite the cantilever purely electrically at first resonance at a fixed static gap z above a point of the sample.
2. Sweep V_{DC} and record the corresponding amplitude A at the first natural frequency using a Lock-In Amplifier (LIA).
3. Repeat this experiment multiple times at different discrete static gaps. Although this can be done continuously providing z increases/decreases sufficiently slowly.

$$\frac{dz}{dt} \approx 0 \quad (10)$$

4. Extract the bias voltage and capacitance gradient corresponding to each static gap by locating the minimum and slope of the A vs V_{DC} curve respectively.

5. Plot $\frac{dC}{dz}$ vs z and curve fit to an analytical expression to extract R .

4. Results and Discussion

The data extracted is shown in figures 1a-1b. Since the SEM image was taken at a tilt of 30 degrees, the radius of the very end of the tip was calculated by measuring the projected radii (as shown in blue and yellow), and extrapolating assuming the tip had an ellipsoid shape.

The experiment as shown by figures 1a-1b extracted a tip radius of $R = 15.3\text{nm}$ whereas an SEM image conducted prior to the experiment showed an effective tip radius of about $R = 18.8\text{nm}$. The supplier for this cantilever type specified a radius $R < 25\text{nm}$. HOPG is conductive and hydrophobic meaning that water layer influence and trapped charges were expected to be minimal. Also, since a fairly low stiffness cantilever was used ($k = 5.52\text{N/m}$), the amplitude in each $A - V_{DC}$ curve is quite high, as expected from equation 6. If the amplitude is too large (relative to the static gap) then the assumption that $\frac{dC}{dz}$ remains constant for each $A - V_{DC}$ curve becomes less accurate. For this reason, it's advised to use harder cantilevers or lower AC voltages.

The effective cone angle and especially the tip height measured in both experiments are not very reliable parameters to extract for small tip sample gaps $z < 200\text{nm}$. This is because the capacitance gradient component for the cone and especially the base of the cantilever are roughly constant over this range of z - and this low sensitivity makes a fitting ineffective. For a more accurate measurement of the cantilever cone angle and tip height, this experiment should be done using static gaps in the order of micrometers.

5. Curve Fitting

Two separate fits were used to extract the tip radius. First, one fit was performed on each set of $A - V_{DC}$ data to extract the bias voltage and $\frac{dC}{dz}$ at each z . Then, the following $\frac{dC}{dz} - z$ data was fitted to the analytical expression from equation 7 to identify the tip radius R , the cone angle θ and the tip height H . First, the amplitude data and DC voltage data ($A_i, V_{DC,i}$) was then fitted to equation 6 using a least squares fitting. The absolute value sign was accounted for by fitting the square of the amplitude. Extracting the parameters $\frac{dC}{dz}$ and $V_s = V_{bias}$ was equivalent to solving the following optimization problem.

$$\min \sum_{i=1}^N \left(A_i^2 - \left(\frac{dC}{dz} V_{AC} Q}{k} (V_{DC,i} - V_s) \right)^2 \right)^2 \quad (11)$$

Following this, each $\frac{dC}{dz}$ and it's corresponding z value were used to fit the analytical expression 7. This was accomplished through another standard least squares minimization.

6. Conclusion

The tip radius of a micro cantilever can be determined using a simplified KPFM technique. This has been demonstrated by comparing an experiment with an SEM image.

This method can also be used to extract other geometries of the cantilever tip as well, provided the experiment is conducted over a large static gap range. The assumptions behind this theory imply that the technique works best with highly conductive, hydrophobic samples with hard cantilevers and low AC tip voltages.

References

- [1] Wilhelm Melitz, Jian Shen, Andrew C. Kummel, and Sangyeob Lee. Kelvin probe force microscopy and its application. *Surface Science Reports*, 66(1):1–27, 2011.
- [2] M Nonnenmacher, MP o'Boyle, and H Kumar Wickramasinghe. Kelvin probe force microscopy. 58(25):2921–2923, 1991.
- [3] Dominik Ziegler and Andreas Force gradient sensitive detection in lift-mode kelvin probe force microscopy. 22(7):075501, 2011.
- [4] S Howell, Debasish Kuila, B Kasibhatla, CP Kubiak, D Janes, and R Reifenberger. Molecular electrostatics of conjugated self-assembled monolayers on au (111) using electrostatic force microscopy. 18(13):5120–5125, 2002.
- [5] Riccardo Borgani, Daniel Forchheimer, Jonas Bergqvist, Per-Anders Thorén, Olle Inganäs, and David B Intermodulation electrostatic force microscopy for imaging surface photo-voltage. 105(14):143113, 2014.
- [6] L Fumagalli, G Gramse, D Esteban-Ferrer, MA Edwards, and G Physics Letters Gomila. Quantifying the dielectric constant of thick insulators using electrostatic force microscopy. 96(18):183107, 2010.
- [7] J Colchero, A Gil, and AM Baró. Resolution enhancement and improved data interpretation in electrostatic force microscopy. *Physical Review B*, 64(24):245403, 2001.
- [8] S Hudlet, M Saint Jean, C Guthmann, and J Berger. Evaluation of the capacitive force between an atomic force microscopy tip and a metallic surface. *The European Physical Journal B-Condensed Matter and Complex Systems*, 2(1):5–10, 1998.
- [9] S Belaidi, P Girard, and G Electrostatic forces acting on the tip in atomic force microscopy: Modelization and comparison with analytic expressions. 81(3):1023–1030, 1997.
- [10] GM Sacha, E Sahagun, and JJ A method for calculating capacitances and electrostatic forces in atomic force microscopy. 101(2):024310, 2007.
- [11] GM Sacha, A Verdaguer, J Martinez, JJ Sáenz, DF Ogletree, and M Physics Letters Salmeron. Effective tip radius in electrostatic force microscopy. 86(12):123101, 2005.
- [12] L Olsson, N Lin, V Yakimov, and R A method for in situ characterization of tip shape in ac-mode atomic force microscopy using electrostatic interaction. 84(8):4060–4064, 1998.
- [13] Huang Wen Hao, AM Baro, JJ Microelectronics, Measurement Nanometer Structures Processing, and Phenomena. Electrostatic and contact forces in force microscopy. 9(2):1323–1328, 1991.
- [14] Jin Moon Choi, Tae Wan Materials. Humidity sensor using an air capacitor. 14(4):182–186, 2013.

Conclusion & Recommendations

4-1 Conclusion

During the course of this project, multiple findings have been documented and significant challenges overcome. Firstly, multiple analytical amplitude and phase equations were derived using different VdW force models. The formulas for both amplitude and phase were validated numerically against a base excitation model. To accomplish this, a robust optimization algorithm based on a modified least squares technique was invented to quickly extract multiple fitting parameters. These formulas were also analyzed statistically to provide an estimate on the upper limit of uncertainty that could be expected when extracting H . These formulas were also compared against each other to provide an understanding of when a comprehensive VdW force model should be used.

To mitigate electrostatic forces during these experiments a simplified KPFM microscopy technique was invented and implemented. This method was later demonstrated to be capable of extracting the tip radius from capacitance gradient data. SEM images validated this method. To accomplish this, another optimization algorithm was invented which could quickly extract the bias voltage and tip radius simultaneously. In addition to this, humidity was found to affect FRCs in certain conditions, highlighting the importance of its mitigation.

Despite significant effort over several months, the method of extracting H through the use of FRCs was not demonstrated reliably through experiment. This was due to unavoidable technical limitations which have been elaborated in section A-5-5.

4-2 Recommendations

I recommend the following avenues of research to anyone who wants to continue work in this field.

4-2-1 Analytical Equation to model Hardening

A successful derivation of analytical equations predicting amplitude and phase in FRCs was derived. However, these formulas are only valid in the attractive regime. I recommend deriving an analytical expression which incorporates the repulsive regime as well. This could, in theory, be used to identify the Young's modulus of the tip/sample.

Unfortunately many tip sample forces are short ranged and extremely difficult to model analytically. Meaning a significant amount of technical work will need to be done to control these external effects.

This is also difficult theoretically because hardening behavior cannot be viewed as a 'small' perturbation. This could invalidate many methods including the method of averaging approach. Similarly, the non-linearity at $d = a_0$ needs to be accounted for.

Nonetheless, method of averaging can overcome issues at $d = a_0$ by integrating over different regions: the purely attractive oscillation region, and part repulsive - part attractive oscillation region. Alternatively, the nondifferentiability can be smoothed out by using the Weierstrass approximation theorem.

4-2-2 Technical Solutions to extracting the Hamaker constant

I have been unable to extract experimentally the Hamaker constant reliably due to three unavoidable technical limitations. Firstly, the sensitivity value was unreliable despite calibration. Secondly, z-fluctuation immediately after positioning the cantilever was present. And thirdly, there exists a large water layer presence on non hydrophobic materials at a humidity of 5%RH or greater.

It will only be possible to extract H experimentally once solutions exist for these technical limitations. In this case, H can only be measured with an upper limit accuracy of $3 \times 10^{-20} J$, and decision would need to be made if this represents an acceptable level of uncertainty. The sensitivity issue was largely a problem because an approximate impedance factor needed to be found to compensate for different voltage signals recorded by the Nanosurf AFM and the MLA. I recommend using a completely new all-in-one system which extracts the raw amplitude signal without the need for an approximate impedance factor. With the current setup, laser alignment can only be done by hand with an Allen key. If the new system can align the laser using software, this will minimize human error. I have presented an equation (A-17) which can extract H without the need for the sensitivity. But it is not as accurate as the formula presented in the papers (A-

7). None the less, these two formulas can be compared against each other to determine whether the new system's sensitivity values are reliable enough to extract H .

It is impossible to completely remove z -fluctuation. However, it can be accounted for. I recommend using an Field-Programmable Gate Array (FPGA) to keep track of the z -fluctuation before and during FRC sweeps. z -fluctuations can be corrected for in post analysis. The affect of humidity was not very noticeable on HOPG because of its hydrophobic nature. However, on many other samples (gold/silicon/tin), unreadable FRCs were produced because of large water layers. If these samples want to be analyzed, an Ultra High Vacuum (UHV) is highly advised.

In all cases, the KPFM method should be used to mitigate electrostatic forces by applying a bias voltage.

4-2-3 Real time tip radius identification

It's theoretically possible, using the simplified KPFM method that I've proposed, that the tip radius can be extracted in real time. This can be done while imaging by using the second natural frequency of the cantilever. This will involve electrically exciting the cantilever tip such that $\omega_{elec} = 6.27\omega_0$ - although $2\omega_{elec} = 6.27\omega_0$ can also be used if the bias voltage is not required during imaging. The capacitance gradient can be extracted in real time while imaging assuming AM-AFM is used at first resonance, and assuming the static gap during imaging is always $< 30\text{nm}$. The advantage of this method is that an operator can measure how the tip is blunting over the course of a separate measurement.

Appendices

Appendix A

A-1 Method of Averaging

Analytical expressions for the amplitude and phase of the FRC were derived so that FRC data could be fitted to extract H . This section details the derivation of these formulas using the method of averaging. One set of equations corresponds to a simplified VdW force, and the other corresponds to the general VdW force.

A-1-1 Simplified Van der Waals force

The one dimensional equation of motion in the most general form can be written as

$$m\ddot{q} + c\dot{q} + kq = F_{ext}(t) + F_{ts,cons}(z + q) + F_{ts,diss}(z + q, \dot{q}) \quad (\text{A-1})$$

To simplify the following calculations, two core assumptions were made: the conservative force was assumed to consist of the purely attractive Van der Waals force $F_{ts,cons} = -\frac{HR}{6(z+q)^2}$, and the dissipative forces were assumed negligible $F_{ts,diss} = 0$. For simplicity, the piezo has been modelled to apply a purely harmonic force $F_{ext} = F_0 \cos(\omega t)$.

Also, making substitutions for the natural frequency far from the sample $\omega_0 = \sqrt{\frac{k}{m}}$ and the quality factor far from the sample $Q = \frac{m\omega_0}{c}$ and substituting into equation A-1 yields

$$\frac{1}{\omega_0^2}\ddot{q} + \frac{1}{\omega_0 Q}\dot{q} + q = \frac{F_0}{k} \cos(\omega t) - \frac{HR}{6k(z+q)^2} \quad (\text{A-2})$$

Using non dimensionalized time $\tau = \omega_0 t$ and non dimensionalized amplitude $x = \frac{q}{z}$ and using the notation $x' = \frac{dx}{d\tau}$ and $x'' = \frac{d^2x}{d\tau^2}$, and assuming all the external forces and damping are sufficiently small such that they can be scaled down by a factor ϵ , the expression becomes

$$x'' + x + \epsilon \left[\frac{1}{Q} x' - \frac{F_0}{zk} \cos\left(\frac{\omega}{\omega_0} \tau\right) + \frac{HR}{6kz^3(1+x)^2} \right] = 0 \quad (\text{A-3})$$

The expression is now in the form allowable to use method of averaging $x'' + x + \epsilon h(x', x, \tau) = 0$. Using this method finds the slowly varying displacement, ie amplitude, r and slowly varying phase ϕ of the tip. The relevant formulas are $\dot{r} = \epsilon < h \sin(\tau - \phi) >$ and $\dot{\phi} = \frac{\epsilon}{r} < h \cos(\tau - \phi) >$ where $x = r \cos(\tau + \phi)$ and $x' = -r \sin(\tau + \phi)$

Also, since the frequency response curve is only desired for drive frequencies near resonance, we can assume $\frac{\omega}{\omega_0} = 1 + \epsilon\sigma$. Also using the simplification that $\theta = \tau + \phi$ and $\alpha = \epsilon\sigma\tau - \phi$, we can write $\cos\left(\frac{\omega}{\omega_0} \tau\right) = \cos(\theta) \cos(\alpha) - \sin(\theta) \sin(\alpha)$. Making this substitution and performing the averaging from 0 to 2π yields

$$\dot{r} = \epsilon \left[-\frac{r}{2Q} + \frac{F_0}{2zk} \sin(\alpha) \right] \quad (\text{A-4})$$

$$\dot{\phi} = \frac{\epsilon}{r} \left[-\frac{HRr}{6kz^3(1-r^2)^{3/2}} - \frac{F_0}{2zk} \cos(\alpha) \right] \quad (\text{A-5})$$

However, it's more convenient to express equation A-5 in terms of the time averaged rate of phase around resonance $\dot{\alpha} = \epsilon\sigma - \dot{\phi}$.

$$\dot{\alpha} = \frac{\epsilon}{r} \left[\sigma r + \frac{HRr}{6kz^3(1-r^2)^{3/2}} + \frac{F_0}{2zk} \cos(\alpha) \right] \quad (\text{A-6})$$

The natural frequency of the system will not remain ω_0 at all static deflections z due to the presence of non linear forces. Recall that since $x = r(\tau) \cos(\tau + \phi(\tau))$ the natural frequency ω_n can be found by setting $F_0 = 0$ and differentiating the argument of the cosine function. Also, since in practice the nonlinear forcing (VDW force) is quite small, $\epsilon = 1$.

$$\begin{aligned}\frac{\omega_n}{\omega_0} &= \frac{d}{d\tau}(\tau + \phi(\tau)) \\ &= 1 - \frac{HR}{6kz^3(1-r^2)^{3/2}}\end{aligned}$$

Coincidentally, this formula also describes the backbone of the frequency response curve (FRC). A complete analytical expression for the FRC, however, can be found by solving for the steady state case ($\dot{r} = 0$ and $\dot{\alpha} = 0$) and solving equations A-4 and A-6 simultaneously.

$$\frac{\omega}{\omega_0} = 1 \pm \frac{1}{2} \sqrt{\left(\frac{F_0}{kzr}\right)^2 - \left(\frac{1}{Q}\right)^2} - \frac{HR}{6kz^3(1-r^2)^{3/2}} \quad (\text{A-7})$$

$$\frac{\omega}{\omega_0} = 1 + \frac{1}{2Q \tan \alpha} - \frac{HRk^2}{6(k^2z^2 - F_0^2Q^2 \sin^2 \alpha)^{3/2}} \quad (\text{A-8})$$

Equation A-7 provides an approximate analytical expression to the FRC where the nondimensionalized frequency is $\frac{\omega}{\omega_0}$ and nondimensionalized amplitude is $r = \max q/z$. Each FRC will be centered around $\frac{\omega}{\omega_0} = 1$ and will exist for values $0 \leq r \leq 1$. Equation A-8 is an approximate analytical for the phase α vs nondimensionalized frequency.

There are several insights A-7 can provide about the nature of the FRC. There is an asymptote at $r = 1$ which corresponds to the unrealistic case where the cantilever tip has penetrated the sample and is experiencing exclusively extremely large Van der Waals forces. The term under the square root sign must be positive resulting in

$$r_{max} = \frac{F_0Q}{kz} < 1 \quad (\text{A-9}) \quad \frac{\omega_{max}}{\omega_0} = 1 - \frac{HRk^2}{6(k^2z^2 - F_0^2Q^2)^{3/2}} \quad (\text{A-10})$$

Where equation A-9 shows the max nondimensionalized amplitude and A-10 shows the corresponding nondimensionalized excitation frequency.

A-1-2 General Van der Waals force

The Van der Waals force used in subsection A-1-1 assumes the only tip surface force present is the simplified Van der Waals force given by equation 1-2. However, this formula is only valid for $R \ll d$. The general expression for this force is given by

$$F_{ts} = -\frac{2HR^3}{3d^2(2R+d)^2} \quad (\text{A-11})$$

Using this expression and following the same steps in section A-1-1 yields a more accurate analytical FRC expression.

$$\frac{\omega}{\omega_0} = 1 \pm \frac{1}{2} \sqrt{\left(\frac{F_0}{kzr}\right)^2 - \left(\frac{1}{Q}\right)^2} - \frac{H}{6kr^2z^3} \left[\frac{(1-r^2)z^4 + 8R^3z + 12R^2z^2 + (6-r^2)Rz^3}{(4R^2 + 4Rz + (1-r^2)z^2)^{3/2}} + \frac{r^2(R+z) - z}{(1-r^2)^{3/2}} \right] \quad (\text{A-12})$$

$$\frac{\omega}{\omega_0} = 1 + \frac{\cot \alpha}{2Q} - \frac{Hk^2}{6F_0^2Q^2 \sin^2 \alpha} \left[\frac{F_0^2Q^2(R+z) \cos^2 \alpha - F_0^2Q^2(R+z) + k^2(2R+z)^3}{(F_0^2Q^2 \cos^2 \alpha - F_0^2Q^2 + k^2(2R+z)^2)^{3/2}} - \frac{k^2z^3 - F_0^2Q^2(R+z) \sin^2 \alpha}{(k^2z^2 - F_0^2Q^2 \sin^2 \alpha)^{3/2}} \right] \quad (\text{A-13})$$

A-2 Sheared fitting function

The one-to-one sheared fitting curve is found by artificially adding the nonlinear component to the amplitude FRC equation.

$$\begin{aligned} \Omega &= 1 \pm \frac{1}{2} \sqrt{\left(\frac{F_0}{kzr}\right)^2 - \frac{1}{Q^2}} - Hf(r, R, k, z) + Hf(r, R, k, z) \\ \Omega &= 1 \pm \frac{1}{2} \sqrt{\left(\frac{F_0}{kzr}\right)^2 - \left(\frac{1}{Q}\right)^2} \\ 4(\Omega - 1)^2 &= \left(\frac{F_0}{zkr}\right)^2 - \left(\frac{1}{Q}\right)^2 \\ r &= \frac{F_0}{kz} \frac{1}{\sqrt{4(\Omega - 1)^2 + \left(\frac{1}{Q}\right)^2}} \end{aligned} \quad (\text{A-14})$$

A-3 Numerical Simulations

Many sets of AUTO simulations were created and fitted. The numerical simulations extract Q and F_0 very accurately. However the high sensitivity of H makes extraction prone to error. Experiments done at large static gaps, where the softening behavior is not so pronounced, are subject to larger errors in H that can be of the order $10^{-19}J$. However, soft cantilevers at low static gaps produce very accurate fits.

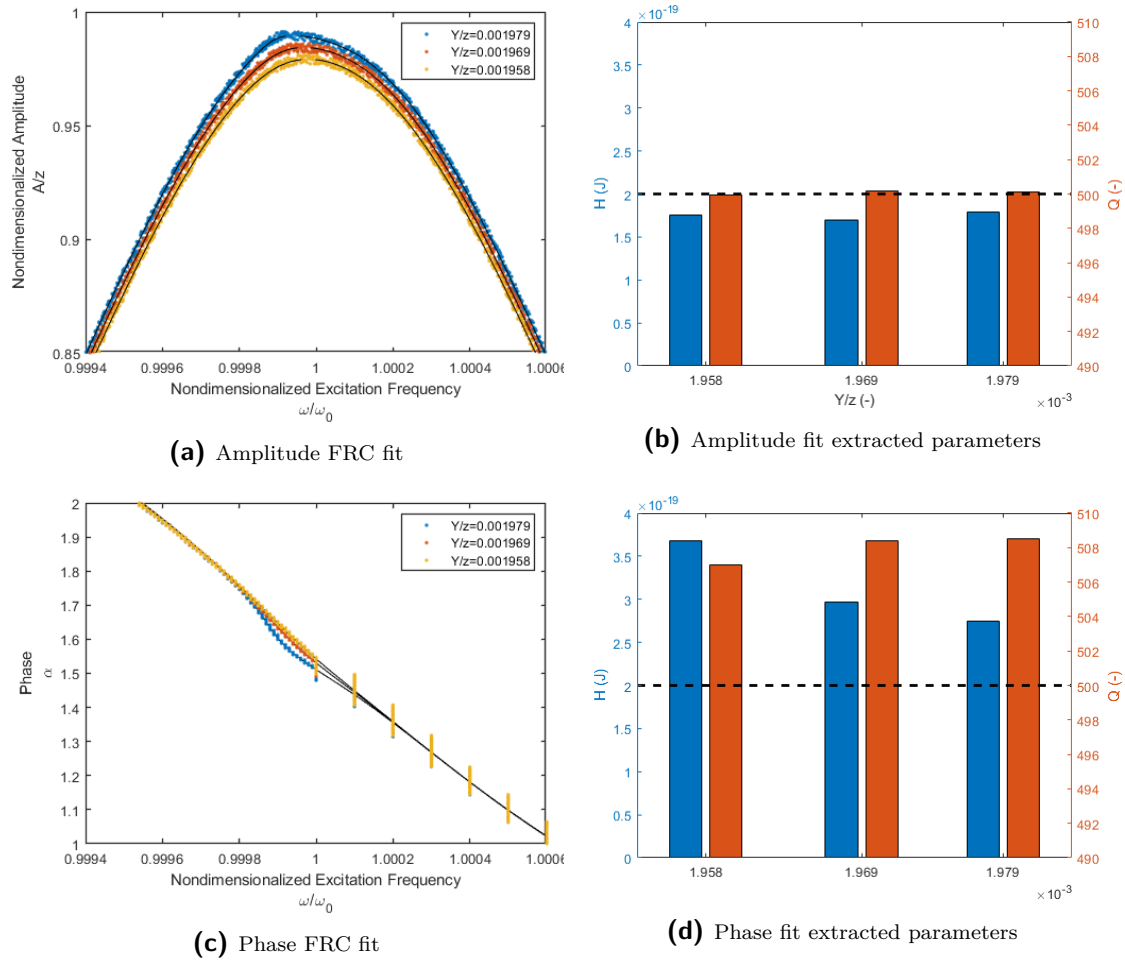


Figure A-1: Fitting 3 numerical FRC data sets (blue/red/yellow) to analytical formulas (black) (with $f = f_1$ and $g = g_1$). The numerical data was generated using a base excitation model with uniformly distributed noise added ($A/z_{noise} = 0.002$). Figures A-1b and A-1d show the extracted parameters from the fits. The effective F_0 extracted for amplitude were 4.7nN, 4.72nN, 4.75nN, and for phase were 4.6nN, 4.63nN, 4.66nN. Values used to generate numerical data, which are also shown by the black dotted line are $k = 24\text{N/m}$, $z = 100\text{nm}$, $R = 150\text{nm}$, $H = 2 \times 10^{-19}\text{J}$, $Q = 500$.

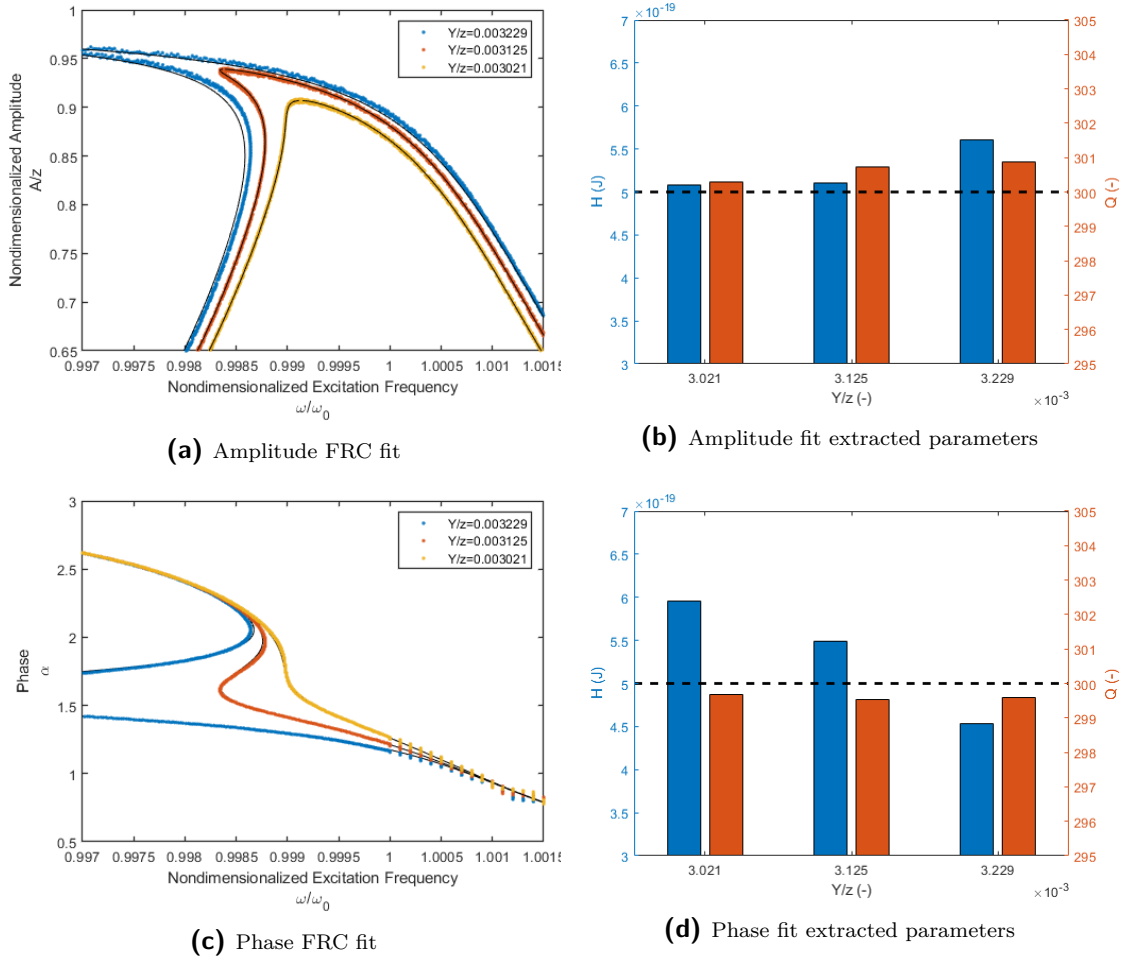


Figure A-2: Fitting 3 numerical FRC data sets (blue/red/yellow) to analytical formulas (black) (with $f = f_1$ and $g = g_1$). The numerical data was generated using a base excitation model with uniformly distributed noise added ($A/z_{noise} = 0.002$). Figures A-11b and A-2d show the extracted parameters from the fits. The effective F_0 extracted for amplitude were 1.45nN, 1.5nN, 1.55nN, and for phase were 1.43nN, 1.5nN, 1.56nN. Values used to generate numerical data, which are also shown by the black dotted line are $k = 24\text{N/m}$, $z = 20\text{nm}$, $R = 150\text{nm}$, $H = 5 \times 10^{-19}\text{J}$, $Q = 300$.

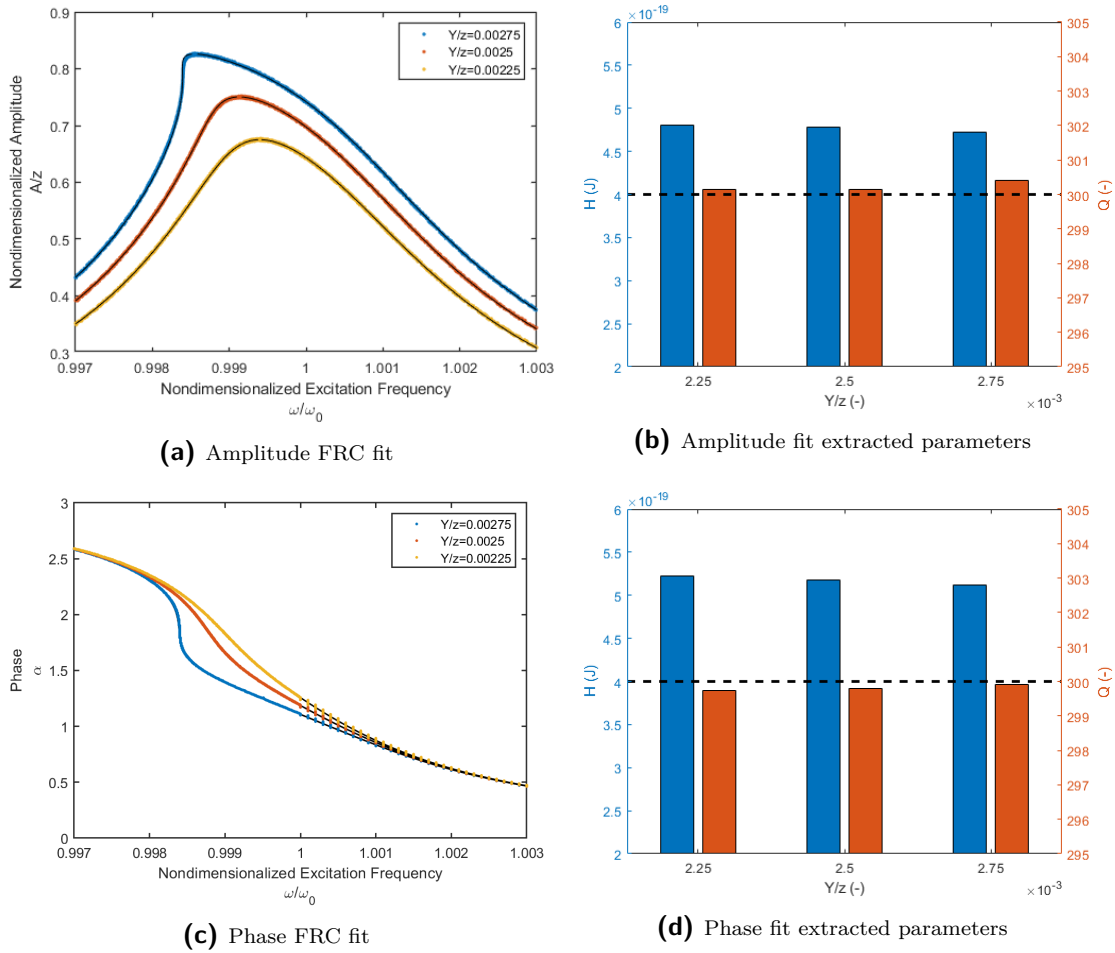


Figure A-3: Fitting 3 numerical FRC data sets (blue/red/yellow) to analytical formulas (black) (with $f = f_1$ and $g = g_1$). The numerical data was generated using a base excitation model with uniformly distributed noise added ($A/z_{noise} = 0.002$). Figures A-3b and A-3d show the extracted parameters from the fits. The effective F_0 extracted for amplitude were 1.8nN, 2nN, 2.2nN, and for phase were 1.76nN, 1.96nN, 2.17nN. Values used to generate numerical data, which are also shown by the black dotted line are $k = 0.2\text{N/m}$, $z = 40\text{nm}$, $R = 50\text{nm}$, $H = 4 \times 10^{-19}\text{J}$, $Q = 300$.

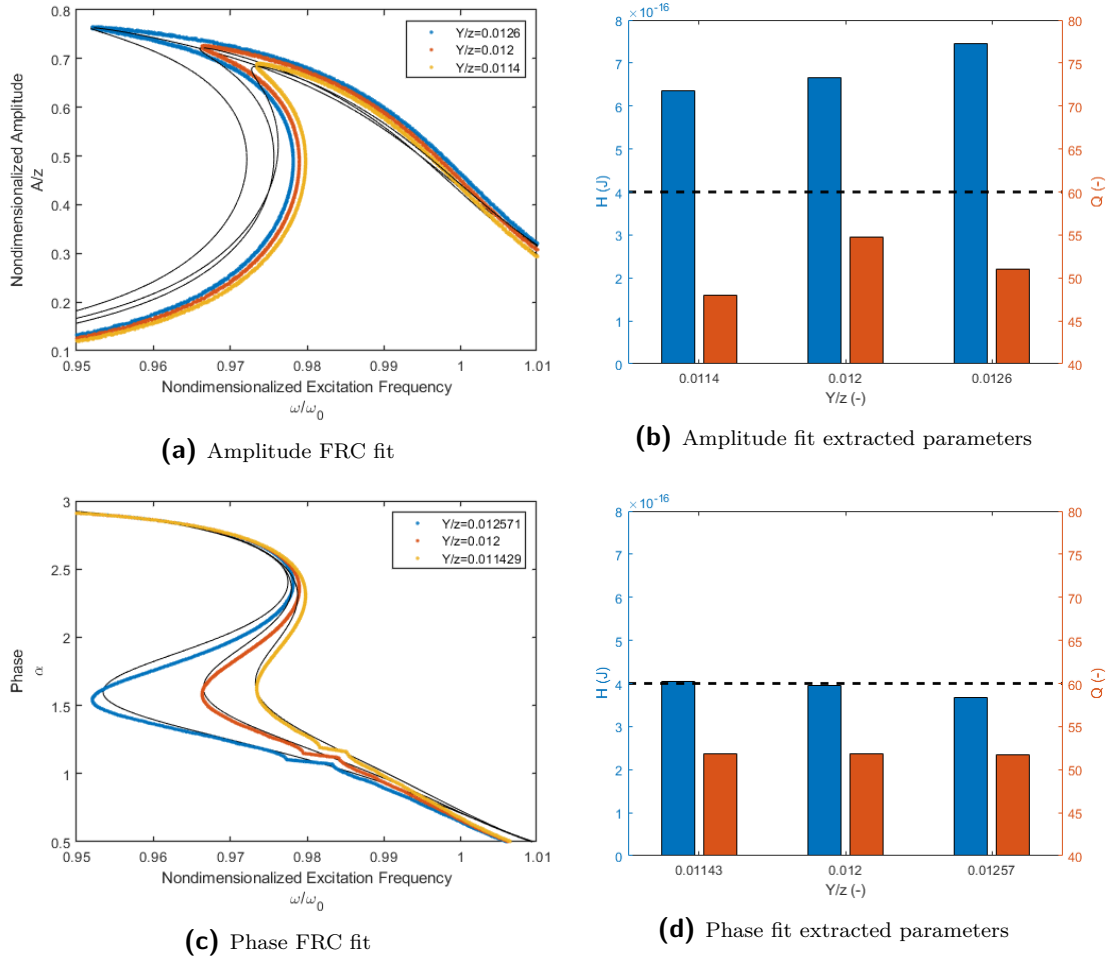


Figure A-4: Fitting 3 numerical FRC data sets (blue/red/yellow) to analytical formulas (black) (with $f = f_1$ and $g = g_1$). The numerical data was generated using a base excitation model with uniformly distributed noise added ($A/z_{noise} = 0.002$). Figures A-7b and A-4d show the extracted parameters from the fits. The effective F_0 extracted for amplitude were 2.5nN, 2.3nN, 2.6nN, and for phase were 2.48nN, 2.61nN, 2.8nN. Values used to generate numerical data, which are also shown by the black dotted line are $k = 5\text{N/m}$, $z = 35\text{nm}$, $R = 30\text{nm}$, $H = 4000 \times 10^{-19}\text{J}$, $Q = 60$.

A-4 Experiments

In the paper, several sets of FRC data were found to have maximum A/z values greater than 1. Figures A-5a and A-5b show two sets of experimental data which demonstrate this.

In figures A-5a and A-5b, multiple FRCs were conducted consecutively, without performing a positioning static displacement curve between each FRC. As can be seen, the softening behavior in the FRCs decrease with time. This is clear evidence of z -fluctuation causing the cantilever to be slowly moved away from the sample. To try and remedy this situation an ‘effective z ’ value for each FRC was generated whereby the maximum non dimensionalized amplitude was forced to be the same as the non dimensionalized amplitude of the first FRC. This is only reasonable assuming the first FRC experiences negligible drift. However, as will be explained in section A-5, issues with z -fluctuation can be significant even for the first FRC. This problem is compounded by inaccuracies in converting the amplitude signal in volts to an amplitude signal in nm. The constant that converts this signal from volts to nm is called the sensitivity (in nm/V), and is determined using a calibration before each experiment.

Additionally, an important observation about figures A-5a and A-5b is that the maximum non dimensionalized amplitude is greater than 1. Both experiments were conducted with a static displacement setpoint of 2nm. Clearly accounting for the static deflection setpoint ($z = 38\text{nm}$ for experiment A-5a and $z = 18\text{nm}$ for experiment A-5b) makes the nondimensionalized amplitude even larger.

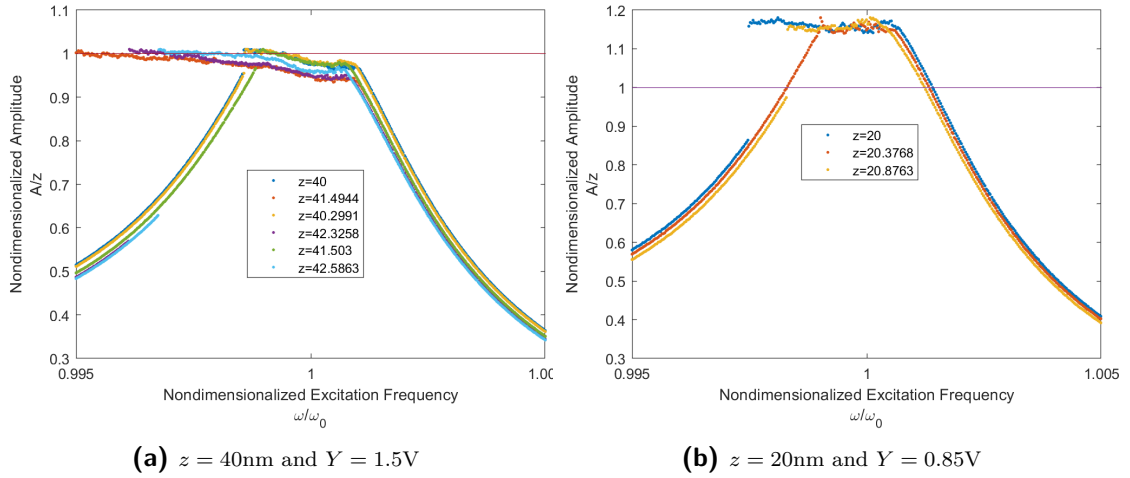


Figure A-5: Additional experiments from the paper showing a non dimensionalized amplitude greater than 1

A-5 Non dimensionalized amplitude methods and phase

A different set of experiments were conducted to explore the technical issues behind the calibrated sensitivity value. Problems associated with the sensitivity were attempted to be resolved by using three different methods of nondimensionalizing amplitude.

Each method analyzes the same data from an experiment conducted with an ElectriTap150-G cantilever and HOPG sample. A hydrodynamic function calibration method was used to extract the following properties. $\omega_0 = 167.16\text{kHz}$, $Q = 348.1$, $k = 6.67\text{N/m}$. The humidity was 4%RH and the temperature at the time of calibration was 22°C .

A-5-1 MLA sensitivity

The nondimensionalized amplitude data $r = \frac{A}{z}$ can be found by multiplying the raw amplitude signal in volts by the sensitivity recorded by the MLA (in nm/V), and dividing by the static gap z . In this set of experiments all non dimensionalized amplitudes calculated using the MLA sensitivity were less than 0.5 despite exhibiting softening behavior.

A-5-2 Nanosurf Sensitivity

Another way of nondimensionalizing amplitude is by using the sensitivity value recorded by the Nanosurf. The nondimensionalizing amplitude r can be found using equation A-15

$$r = \frac{A}{z} = \frac{A_{MLA}(V)}{A_{max,MLA}(V)} \times \frac{A_{max,ns}(V) \times \text{sensitivity}_{ns}}{z} \quad (\text{A-15})$$

The left term can be found by dividing the raw amplitude signal recorded by the MLA $A_{MLA}(V)$ by the maximum amplitude of the signal $A_{max,MLA}(V)$.

The experiments shown in figures A-6a - A-6d and figures A-7a - A-7f are fitted using the nondimensionalized amplitude calculated using the Nanosurf sensitivity.

A-5-3 Amplitude Ratio

A revised formula was made in which the nondimensionalized amplitude no longer defined to be a ratio of amplitude to static gap. Instead, the nondimensionalized amplitude \bar{A} was defined as the ratio of the raw amplitude signal (in volts) divided by the maximum amplitude (in volts). Hence avoiding the need for a sensitivity all-together.

The maximum amplitude of a FRC for the nonlinear case is the same as the linear case and is given by $\frac{F_0 Q}{k}$.

$$\bar{A} = \frac{A(V)}{A_{max}(V)} = \frac{A \times \text{sensitivity}}{A_{max} \times \text{sensitivity}} = \frac{k}{F_0 Q} A = \frac{kz}{F_0 Q} r \quad (\text{A-16})$$

The revised FRC equation in terms of \bar{A} is given by equation A-17.

$$\Omega = 1 \pm \frac{1}{2Q} \sqrt{\frac{1}{\bar{A}^2} - 1 - Hf\left(\frac{F_0 Q}{kz} \bar{A}, R, k, z\right)} \quad (\text{A-17})$$

Equation A-17 shows the peak of the FRC at $\bar{A}_{peak} = 1$ (by definition) and $\Omega_{peak} = 1 - f\left(\frac{F_0 Q}{kz}, R, k, z\right)$. While this equation has the added advantage of avoiding the need for calibrating sensitivity, it comes with the disadvantage of removing the usefulness of the amplitude peak - which had previously made curve fitting for F_0 very effective. Instead F_0 exists purely in the nonlinear term, which can make curve fitting for H more challenging.

The experiments shown in figures A-8a - A-8d and figures A-9a - A-9f are fitted using the nondimensionalized equation A-17.

A-5-4 Phase

Another way to avoid using the sensitivity value to fit experimental data was to use phase data instead. The experiments shown in figures A-10a - A-10d and figures A-11a

- A-11f are fitted using equation A-13.

A-5-5 Experiment Discussion

An analysis of the different methods attempted to resolve the issue of unreliable calibrated sensitivity have been outlined below. Relevant technical issues are also commented on.

The experiments analyzed using a sensitivity recorded by the MLA are unreliable since the nondimensionalized amplitude was far less than 1 for all curves. A large reason for this is because the deflection data was transferred from the AFM to the MLA. An impedance factor had to be calibrated to ensure that the deflection recorded by the AFM matched the deflection recorded by the MLA. This was accomplished by multiplying the amplitude of the deflection data recorded by the MLA by a constant such that it matched the amplitude of the deflection data recorded by the AFM software. Both the MLA and AFM had their own separate inbuilt oscilloscopes. The calibrated impedance factor was found to be approximately 1.22. The uncertainty in the impedance factor proportionally affected the amplitude output in nm, resulting in nondimensionalized amplitudes slightly higher or lower than expected. Additionally, other sources of errors originate from the manual alignment of the laser on the cantilever tip. This misalignment strongly affects the sensitivity recorded by the MLA. In theory, this shouldn't be a large cause of error since the amplitude signal in volts should also be scaled up/down by the same factor as the sensitivity. However, misalignment of the laser could cause problems with short cantilevers on highly reflective surfaces. If the laser is reflecting from a point of the cantilever which is closer to one of its nodes, then the measured amplitude will be less than the deflection of the tip. Additionally, any light reflecting off a highly reflective surface at low static gaps can interfere with the measurement recorded by the photo diode.

Nondimensionalizing amplitude using the sensitivity from the Nanosurf AFM managed to improve the quality of the FRCs significantly. Many of the nondimensionalized amplitudes are very close to 1, as expected, facilitating good fits to be made. However, there are still several issues with using method of nondimensionalizing. Firstly, the sensitivity recorded by the AFM uses a deflection calibration from static displacement curves. This is expected to be less accurate than a thermal calibration analyzed around the first eigenfrequency. Additionally, the Nanosurf software does not have an inbuilt feature to export amplitude signal data. This is an issue because the amplitude signal had to be observed manually in real time from a small monitoring tab. Unavoidable human error made accurately recording the $A_{max,MLA}(V)$ value impossible. The low dimensionless amplitude shown in figures A-7d and A-7f illustrate this. In these cases, the static gap was increased and the real amplitude of the cantilever is much larger due to the increased forcing. However, the monitoring tab displayed an amplitude that appeared to remain roughly constant, leading to an unrealistically low softening behavior at low nondimensionalized amplitudes. Consequently, the nondimensionalized ampli-

tude values were unrealistically small. Additionally, evidence for z-fluctuation can be seen observed in figure A-7e. This figure shows a completely linear response, whereas identical experiments at the same positioned static gap and base excitation show very different FRC shapes. This is likely due to thermal fluctuations and piezo creep moving the cantilever tip sufficiently far away from the sample before a FRC was created. All FRCs were conducted immediately after positioning the cantilever, which implies that significant z-fluctuations can occur during the course of the positioning static displacement curve. This is further evidenced by the F_0/Y ratios not being constant across the FRCs. Additionally, figure A-7e has been fitted with a very large H . This large value is very likely a result of a slight error recorded in the true natural frequency far from the sample ω_0 . This could be caused by the cantilever tip attracting water during the positioning static displacement. The effective added mass will reduce ω_0 . Using a manually adjusted ω_0 for all FRCs such that the fitted H in figure A-7e was a minimum, did not resolve the fluctuating H and F_0 values observed.

Nondimensionalizing amplitude using the refined A/A_{max} equation A-17 solves the sensitivity issue, but uses a less robust equation to output fitting parameters. Nonetheless, this method can fit data corresponding to figures A-9d and A-9f, adding further evidence that poor quality fits from figures A-7d and A-7f were caused by a sensitivity error. The H extracted from these fits vary significantly, with most in the order of $10^{-17}J$. Interestingly, the H extracted increased with larger tip sample gap z on average. This is an unrealistic result and is speculated to be caused by the optimization algorithm (which is based on equation A-17) mistaking a decreased excitation force for an increased H . A similar problem is observed in figure A-9e. A completely linear FRC with a nondimensionalized amplitude of 1, makes extracting F_0 reliably impossible. This is because using equation A-17, F_0 can only be extracted from the influence of softening. An additional complication is that the z-fluctuation cannot be easily observed using this method because, unlike the previous methods, the nondimensionalized amplitude is never greater than 1.

The phase fitting scheme share the same problems as equation A-17. Additionally, the offset fitting parameter make the optimization algorithm less robust. In many cases, the phase was poorly fitted because several local minima in the least squared error caused the optimization algorithm to end prematurely. Despite this figure A-11e adds further evidence of z-fluctuation due to its linear relationship.

Each experiment was conducted with a set of FRCs that had a bias voltage, and a control set of FRCs that did not have a bias voltage. The influence of a bias voltage mitigates the attractive electrostatic force, and should decrease the softening behavior. However, each experiment appears to show no reliable difference between FRC sets. This is likely due to the experimental setup limitations described.

A-6 Experimental FRC fits

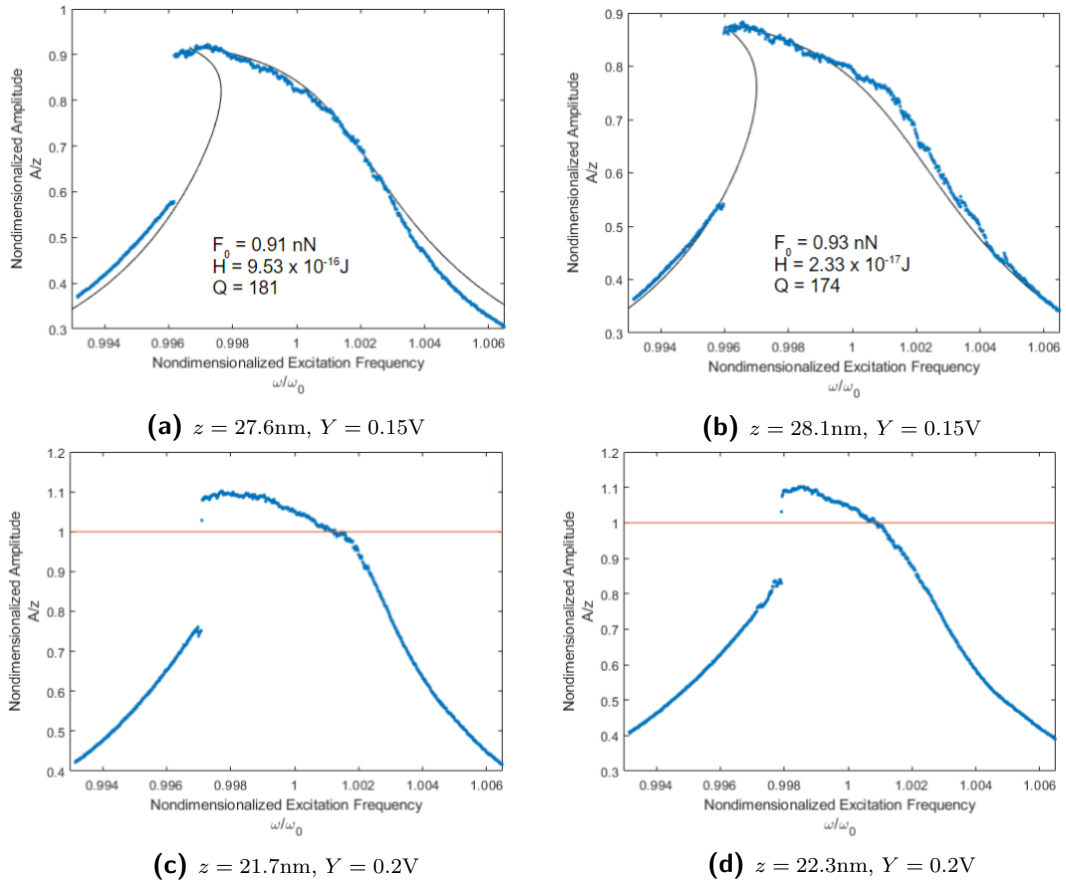


Figure A-6: Amplitude FRC's with a bias voltage of 1.1V. Amplitude FRCs fitted using the nondimensionalized amplitude $\frac{A}{z}$ determined using the sensitivity value recorded by the Nanosurf. Some curves show a nondimensionalized amplitude greater than 1

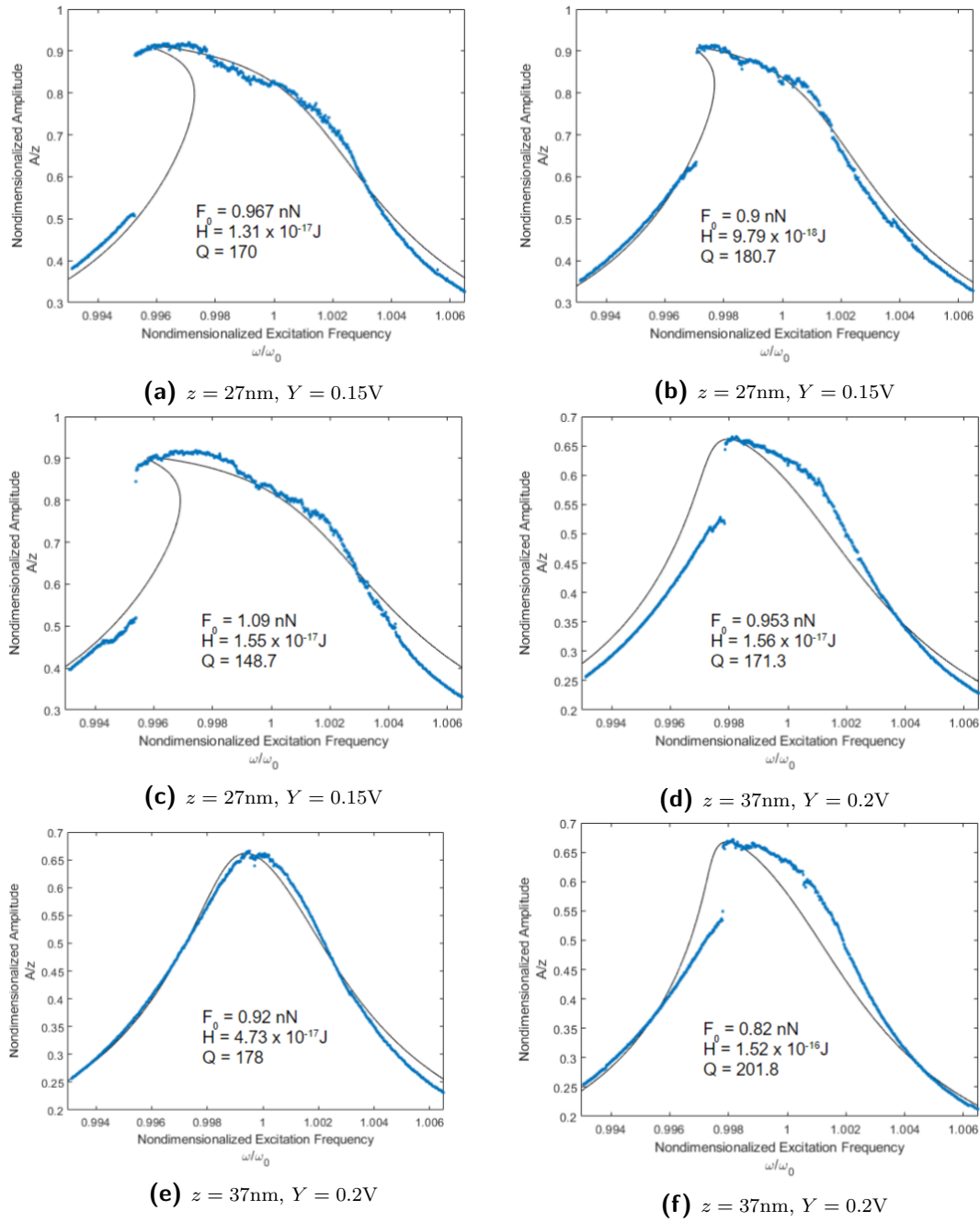


Figure A-7: Amplitude FRC's without a bias voltage applied. Amplitude FRCs fitted using the nondimensionalized amplitude $\frac{A}{z}$ determined using the sensitivity value recorded by the Nanosurf. Some curves appear linear while others show softening at unrealistically low nondimensionalized amplitudes

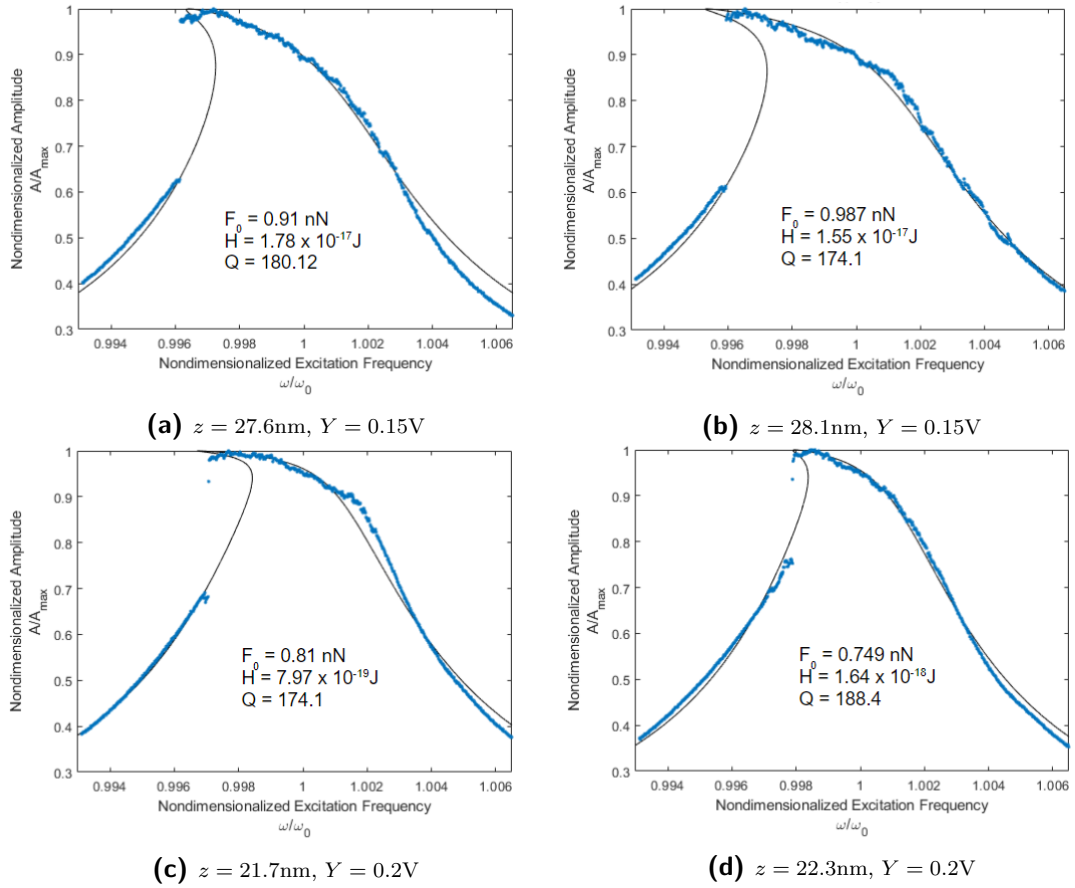


Figure A-8: Amplitude FRC's with a bias voltage of 1.1V. Amplitude FRCs fitted using the nondimensionalized amplitude $\frac{A}{A_{max}}$ from equation A-17. H and F_0/Y values vary significantly

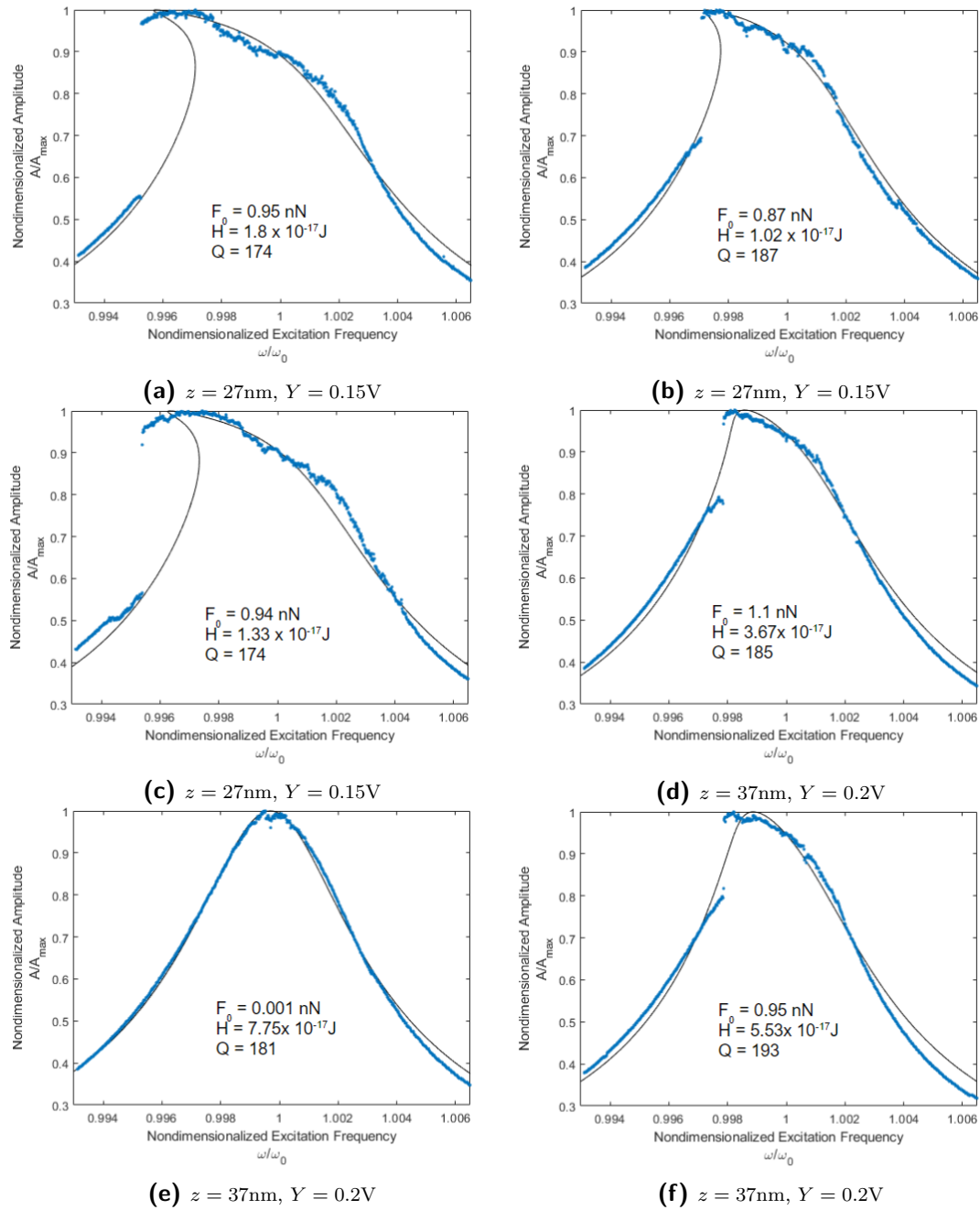


Figure A-9: Amplitude FRC's without a bias voltage. Amplitude FRCs fitted using the nondimensionalized amplitude $\frac{A}{A_{max}}$ from equation A-17. H and F_0/Y values vary significantly

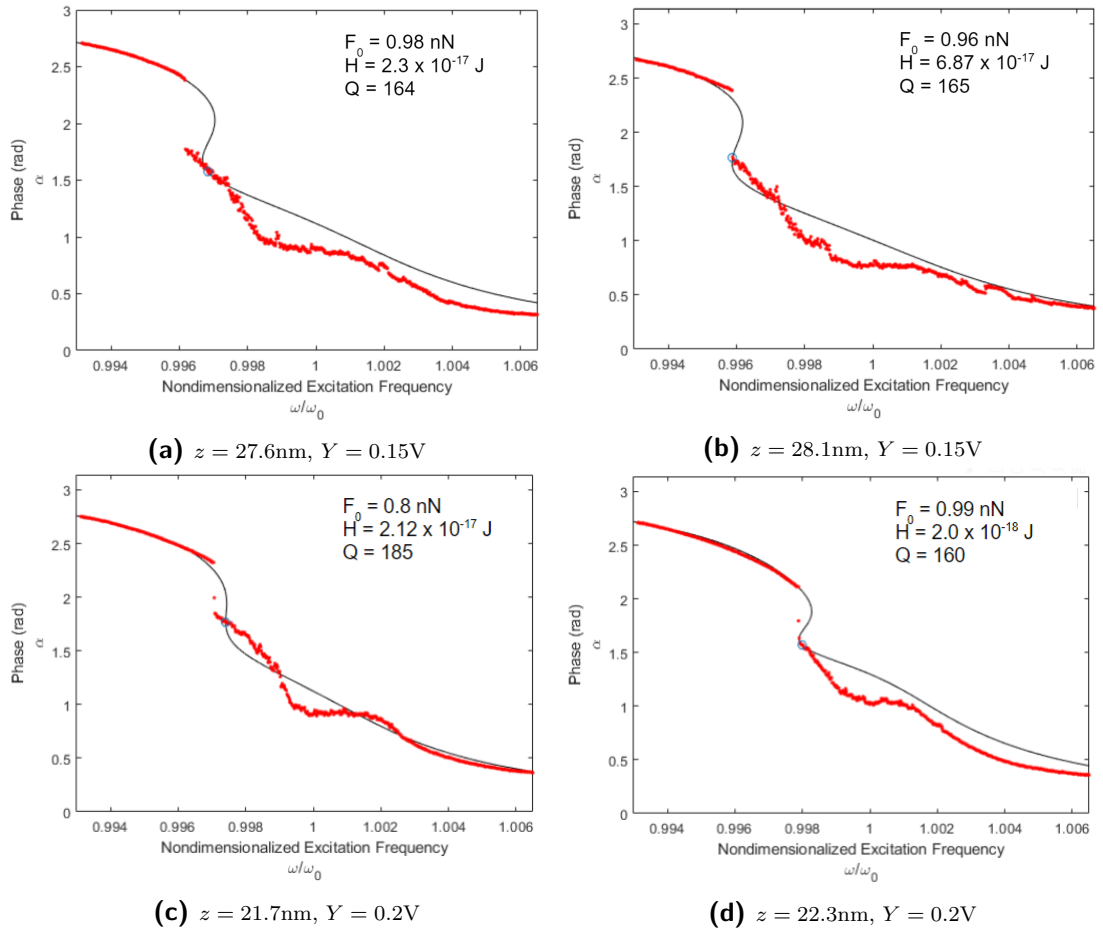


Figure A-10: Phase FRC's with a bias voltage of 1.1V. H and F_0/Y values vary significantly

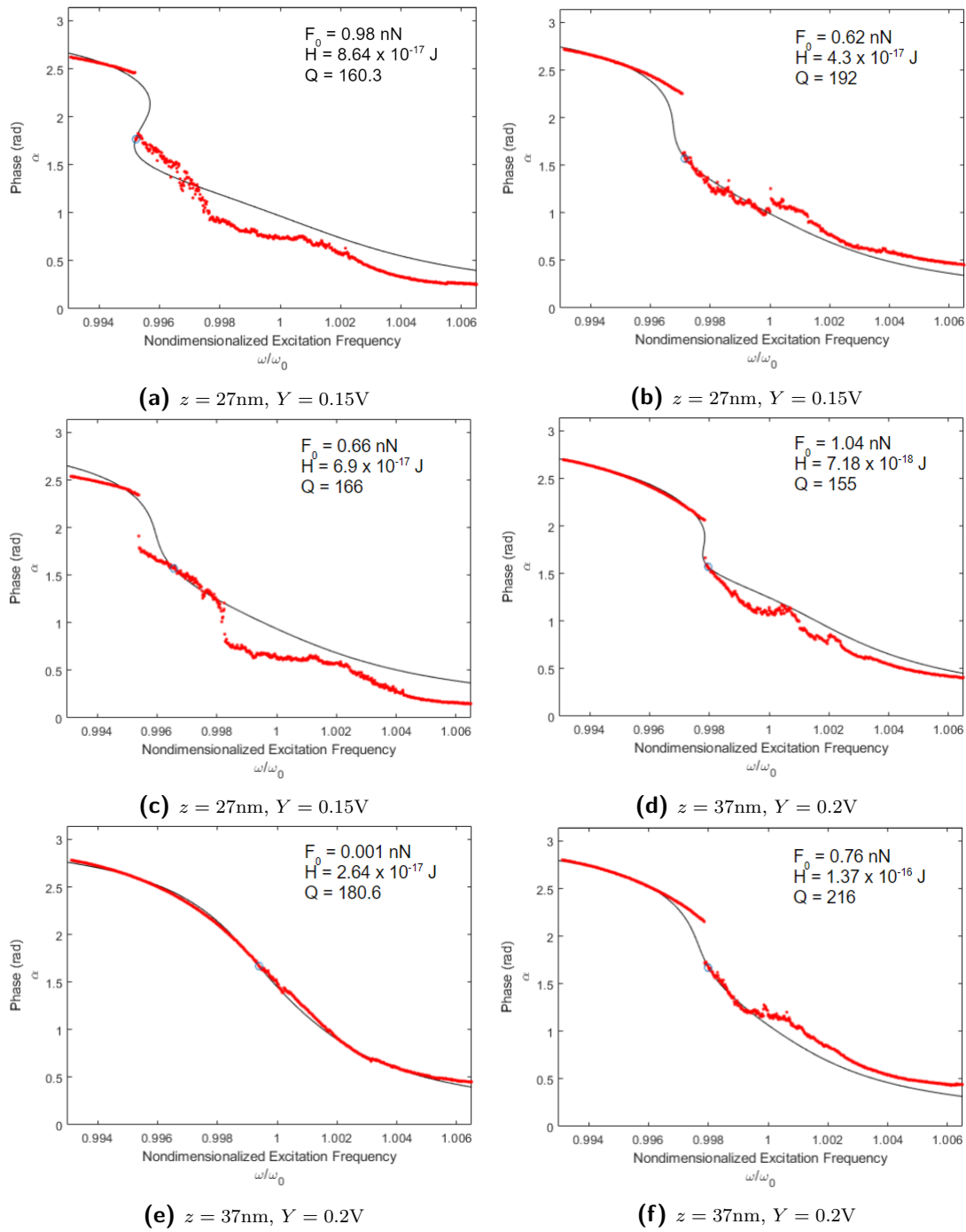


Figure A-11: Phase FRC's without a bias voltage. H and F_0/Y values vary significantly

A-7 Humidity affects on experiments

In practice, humidity in the air can cause small water layers to form on the surface of a sample and cantilever tip. When the tip gets sufficiently close to the sample, a water neck can occur. This water neck is adhesive in nature and depends strongly on the geometry of the cantilever tip [37]. This water neck breaks off at larger tip sample gaps than when it formed, leading to dissipation and hysteresis

An experiment was conducted to see the influence humidity can have on the FRC's. A silicon sample was placed in a humidity chamber at 5% real humidity (RH). The lid was then opened, causing the humidity to equilibrate to the humidity of the room (37%RH). Multiple static deflection curves on approach were recorded in real time as the humidity increased. The static deflection q^* was multiplied by the stiffness of the cantilever $k = 24.1\text{N/m}$ to provide the tip sample force F_{ts} .

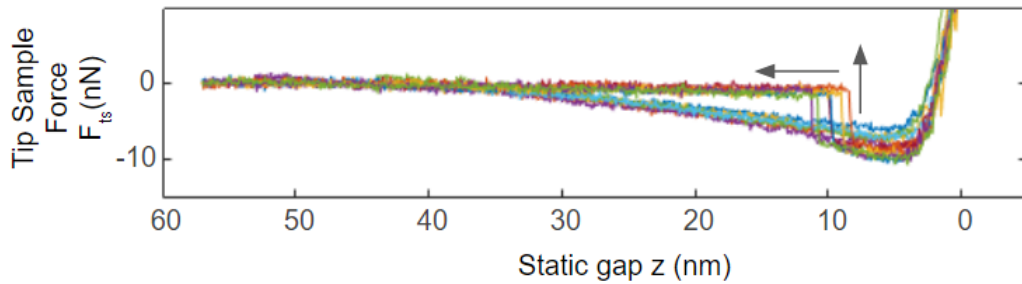


Figure A-12: Consecutive approach static deflection curves over time. Shortly after opening the humidity chamber snap-in is observed. As time passes, snap-in occurs at larger static gaps.

Figure A-12 shows that the humidity values at least greater than 5% on a silicon surface affects the force-distance curve significantly. As the humidity increases, a snap-in is observed which is likely indicative of a water neck forming. Also, as humidity increases even more, the snap-in occurs further away from the sample, likely indicating an increase in water layer thickness.

Even though silicon is hydrophobic, a silicon oxide layer had likely formed on the surface during these experiments, making the surface hydrophilic. Consequently, no conclusions can be drawn about the influence of humidity on truly hydrophobic samples like HOPG in humidity values less than 5% RH.

Appendix B

B-1 Capacitance gradient analytical model

The total capacitance between the tip and sample is made up from 3 distinct components. These components include the tip apex, the the tip cone and the lever.

$$\frac{dC}{dz} = \frac{dC}{dz}_{apex} + \frac{dC}{dz}_{cone} + \frac{dC}{dz}_{lever} \quad (\text{B-1})$$

Analytical approximations for each of these components have been made and are available in the literature [16] [38].

$$\frac{dC}{dz}_{apex} = \frac{-2\pi\epsilon \left(R + \frac{z}{2}\right)^2 \left(\frac{R-2z}{z \left(\frac{2z \tan^2(\frac{\theta}{2})}{R} + 1 \right)} + 2 \log \left(\frac{4z}{\cos(\theta)(R-2z)+R+2z} \right) \right)}{(R-2z)^2 \left(\frac{z^2 \log(\csc(\frac{\theta}{2}))}{R^2 (1-\sin(\frac{\theta}{2})) (\sin(\frac{\theta}{2})+3)} + 1 \right)} \quad (\text{B-2})$$

$$\frac{dC}{dz}_{cone} = \frac{-8\pi\epsilon \left(\log \left(\frac{H - \frac{1}{2}R \cot^2(\frac{\theta}{2}) + z}{\frac{1}{2}R \cot^2(\frac{\theta}{2}) + z} \right) - \frac{\sin(\frac{\theta}{2})(H - R \cot^2(\frac{\theta}{2}))(z - \frac{1}{2}R \cot^2(\frac{\theta}{2}))}{(\frac{1}{2}R \cot^2(\frac{\theta}{2}) + z)(H - \frac{1}{2}R \cot^2(\frac{\theta}{2}) + z)} \right)}{(\pi - \theta)^2} \quad (\text{B-3})$$

$$\approx \frac{-8\pi\epsilon \left(\log \left(\frac{2H \tan^2(\frac{\theta}{2})}{R} \right) + \sin \left(\frac{\theta}{2} \right) \right)}{(\pi - \theta)^2} \quad (\text{B-4})$$

$$\frac{dC}{dz_{\text{lever}}} = \frac{-4\epsilon Lw \tan^2\left(\frac{\theta_L}{2}\right)}{\theta_L^2 (H+z)^2 \left(\frac{2L \tan\left(\frac{\theta_L}{2}\right)}{H+z} + 1\right)} \quad (\text{B-5})$$

$$\approx \frac{-4\epsilon Lw \tan^2\left(\frac{\theta_L}{2}\right)}{H\theta_L^2 \left(H + 2L \tan\left(\frac{\theta_L}{2}\right)\right)} \quad (\text{B-6})$$

Where θ_L is the angle the lever makes from the horizontal, H = tip height, L = cantilever length, w = cantilever width, and θ = cone angle.

Appendix C

C-1 Cantilever dynamics Theory

The cantilever dynamics are adequately approximated by Euler Bernoulli beam theory. This approximation is valid because the length of the cantilever is considerably large (in the order of $100\mu\text{m}$) whereas the amplitude of oscillation is quite small (in the order of 10nm). The equation of motion is given by C-1, where f is the external force per unit length.

$$\rho A \ddot{w} + EI w'''' = f \quad (\text{C-1})$$

The natural frequencies and mode-shapes of this beam can be found by setting $f = 0$ and assuming a solution in the form $w = W(x)e^{i\Omega t}$.

$$\begin{aligned} -\Omega^2 \rho A W(x) e^{i\Omega t} + EI W(x)'''' e^{i\Omega t} &= 0 \\ -\Omega^2 \rho A W(x) + EI W(x)'''' &= 0 \end{aligned}$$

And now defining the term $\beta^4 = \frac{\rho A}{EI} \Omega^2$ and solving for the mode-shape $W(x)$ yields

$$\begin{aligned} W(x)'''' - \beta^4 W(x) &= 0 \\ W(x) &= c_1 e^{\beta x} + c_2 e^{-\beta x} + c_3 e^{\beta x i} + c_4 e^{-\beta x i} \\ W(x) &= A \cosh \beta x + B \sinh \beta x + C \cos \beta x + D \sin \beta x \end{aligned}$$

AFM's are typically modelled as a clamped - free connection. This implies the following $w(0, t) = 0$, $w(0, t)' = 0$, $w(L, t)'' = 0$, $w(L, t)''' = 0$. Inserting these boundary conditions into the equation for $W(x)$ will force the following result $\cos \beta L = \frac{-1}{\cosh \beta L}$. Solving this numerically produces an infinite number of values for β : $\beta_1 \approx \frac{1.875}{L}$, $\beta_2 \approx \frac{4.694}{L}$, etc. Each of these values can be rearranged to find the corresponding natural frequency.

$$\Omega_1 \approx \frac{3.52}{L^2} \sqrt{\frac{EI}{\rho A}}$$

$$\Omega_2 \approx 6.27 \times \Omega_1 \approx \frac{22.03}{L^2} \sqrt{\frac{EI}{\rho A}}$$

The boundary conditions also eliminate 3 of the 4 constants, producing the following result

$$W(x) = A \left[\cosh \beta x - \frac{\cosh \beta L + \cos \beta L}{\sinh \beta L + \sin \beta L} \sinh \beta x - \cos \beta x + \frac{\cosh \beta L + \cos \beta L}{\sinh \beta L + \sin \beta L} \sin \beta x \right]$$

Since there are an infinite number of natural frequencies Ω_n , there are also an infinite number of corresponding mode-shapes $W_n(x)$. Using superposition and recalling that $w(x, t) = W(x)e^{i\Omega t}$, the general solution can be written as

$$w(x, t) = \sum_{n=1}^{\infty} W_n(x)e^{i\Omega_n t}$$

$$w(x, t) = \sum_{n=1}^{\infty} A_n \left[\cosh \beta_n x - \frac{\cosh \beta_n L + \cos \beta_n L}{\sinh \beta_n L + \sin \beta_n L} \sinh \beta_n x - \cos \beta_n x + \frac{\cosh \beta_n L + \cos \beta_n L}{\sinh \beta_n L + \sin \beta_n L} \sin \beta_n x \right] \sin(\Omega_n t + \phi_n)$$

The constants A_n and ϕ_n can be found using initial conditions. This formula is quite complicated and difficult to use analytically. Typically, Engineers approximate this expression by assuming all modes $n \geq 2$ are negligible. This is a reasonable approximation since in most AFM's the tip is excited near the first resonance only. It's also convenient to model the entire motion of the very tip of the cantilever as an equivalent spring mass damper with mass m and stiffness k . Since the tip is assumed to oscillate at the first mode exclusively, $\Omega_1 = \sqrt{\frac{k}{m}}$.

However, another equation is needed to find the equivalent stiffness k . This is done by considering the same beam in static equilibrium where an equivalent spring force $F = k \times w(L)$ is acting on the free end.

$$EIw_{static}''''(x) = F\delta(x - L)$$



Figure C-1: Equivalent cantilever beam with a point force acting on its end F

The boundary conditions; $w_{static}(0) = 0$, $w'_{static}(0) = 0$, $-EIw''_{static}(L) = 0$ and $-EIw'''_{static}(L) = F$ yield the final static displacement equation

$$w_{static}(x) = \frac{-F}{6EI}x^3 + \frac{FL}{2EI}x^2$$

The equivalent force is now $F = k \times w_{static}(L) = k \times \frac{FL^3}{3EI}$. Solving for k , and substituting this value of k into the expression $\Omega_1 = \frac{3.52}{L^2} \sqrt{\frac{EI}{\rho A}} = \sqrt{\frac{k}{m}}$ yields the following results. Note the mass of the cantilever is $m_c = \rho AL$

$$k = \frac{3EI}{L^3}$$

$$m \approx 0.242m_c$$

Bibliography

- [1] G. Binnig, C. F. Quate, and Ch. Gerber. Atomic force microscope. *Phys. Rev. Lett.*, 56:930–933, Mar 1986.
- [2] Ricardo Garcia and Rubén Pérez. Dynamic atomic force microscopy methods. *Surface Science Reports*, 47(6):197–301, 2002.
- [3] Ronald G Reifenberger. *Fundamentals of Atomic Force Microscopy: Part I: Foundations*. World Scientific Publishing Company Pte Limited, 2016.
- [4] Brunero Cappella and Giovanni Dietler. Force-distance curves by atomic force microscopy. *Surface science reports*, 34(1-3):1–104, 1999.
- [5] J. N. Munday. Measured long-range repulsive casimirlifshitz forces. *Nature*, 457(7226):170, 2009.
- [6] Daniel Forchheimer, Daniel Platz, Erik A Tholén, and David B Haviland. Simultaneous imaging of surface and magnetic forces. *Applied Physics Letters*, 103(1):013114, 2013.
- [7] Riccardo Borgani, Daniel Forchheimer, Jonas Bergqvist, Per-Anders Thorén, Olle Inganäs, and David B Intermodulation electrostatic force microscopy for imaging surface photo-voltage. 105(14):143113, 2014.
- [8] Mahdi Farshchi-Tabrizia, Michael Kappl, and Hans-Jürgen Butt. Influence of humidity on adhesion: an atomic force microscope study. *Journal of Adhesion Science*

- and Technology*, 22(2):181–203, 2008.
- [9] Tim J Senden, Calum J Engineering Aspects. Surface chemistry and tip-sample interactions in atomic force microscopy. 94(1):29–51, 1995.
- [10] Brad A Krajina, Lakshmi S Kocherlakota, and René M chemical physics Overney. Direct determination of the local hamaker constant of inorganic surfaces based on scanning force microscopy. 141(16):164707, 2014.
- [11] Hideki Miyazaki and Tomomasa Mechanical assembly of three-dimensional microstructures from fine particles. 11(2):169–185, 1996.
- [12] S. Hu. Frequency domain identification of tip-sample van der waals interactions in resonant atomic force microcantilevers. *Journal of Vibration and Acoustics*, 126(3):343, 2004.
- [13] J On hamaker constants: A comparison between hamaker constants and lifshitz-van der waals constants. 3(4):331–363, 1972.
- [14] Raymond R Dagastine, Dennis C Prieve, Lee R interface science. Calculations of van der waals forces in 2-dimensionally anisotropic materials and its application to carbon black. 249(1):78–83, 2002.
- [15] Gerard Jan Verbiest. *Unravelling heterodyne force microscopy*. Leiden University Press, 2013.
- [16] J Colchero, A Gil, and AM Baró. Resolution enhancement and improved data interpretation in electrostatic force microscopy. *Physical Review B*, 64(24):245403, 2001.
- [17] Daniel Kiracofe, John Melcher, and Arvind Raman. Gaining insight into the physics of dynamic atomic force microscopy in complex environments using the veda simulator. *Review of Scientific Instruments*, 83(1):013702, 2012.
- [18] Miquel Salmeron, Lei Xu, Jun Hu, and Qing Dai. High-resolution imaging of liquid structures: Wetting and capillary phenomena at the nanometer scale. *MRS Bulletin*, 22(8):36–41, 1997.
- [19] 2018.
- [20] Elena T Herruzo and Ricardo Garcia. Frequency response of an atomic force microscope in liquids and air: Magnetic versus acoustic excitation. *Applied Physics Letters*, 91(14):143113, 2007.

-
- [21] Sebastian Rützel, Soo Il Lee, and Arvind Raman. Nonlinear dynamics of atomic-force-microscope probes driven in lennard-jones potentials. In *Proceedings of the Royal Society of London A: Mathematical, Physical and Engineering Sciences*, volume 459, pages 1925–1948. The Royal Society.
- [22] SI Lee, SW Howell, Av Raman, and R Reifengerger. Nonlinear dynamics of micro-cantilevers in tapping mode atomic force microscopy: A comparison between theory and experiment. *Physical Review B*, 66(11):115409, 2002.
- [23] Alvaro San Paulo and Ricardo Garcia. Unifying theory of tapping-mode atomic-force microscopy. *Physical Review B*, 66(4):041406, 2002.
- [24] Mehdi Ayat, Mohammad Amin Karami, Sattar Mirzakuchaki, and Aliasghar Beheshti-Shirazi. Design of multiple modulated frequency lock-in amplifier for tapping-mode atomic force microscopy systems. *IEEE Transactions on Instrumentation and Measurement*, 65(10):2284–2292, 2016.
- [25] Wilhelm Melitz, Jian Shen, Andrew C. Kummel, and Sangyeob Lee. Kelvin probe force microscopy and its application. *Surface Science Reports*, 66(1):1–27, 2011.
- [26] M Nonnenmacher, MP o’Boyle, and H Kumar Wickramasinghe. Kelvin probe force microscopy. 58(25):2921–2923, 1991.
- [27] U Hartmann. van der waals interactions between sharp probes and flat sample surfaces. *Physical Review B*, 43(3):2404, 1991.
- [28] Sean G Fronczak, Christopher A Browne, Elizabeth C Krennek, Stephen P Beaudoin, and David S Corti. Non-contact afm measurement of the hamaker constants of solids: Calibrating cantilever geometries. *Journal of colloid and interface science*, 517:213–220, 2018.
- [29] Soma Das, PA Sreeram, and AK Raychaudhuri. A method to quantitatively evaluate the hamaker constant using the jump-into-contact effect in atomic force microscopy. *Nanotechnology*, 18(3):035501, 2007.
- [30] Sean G Fronczak, Jiannan Dong, Christopher A Browne, Elizabeth C Krennek, Elias I Franses, Stephen P Beaudoin, and David S Corti. A new “quasi-dynamic” method for determining the hamaker constant of solids using an atomic force microscope. *Langmuir*, 33(3):714–725, 2017.
- [31] Ludwig Reimer. *Scanning electron microscopy: physics of image formation and microanalysis*, volume 45. Springer, 2013.

- [32] S Hudlet, M Saint Jean, C Guthmann, J B-Condensed Matter Berger, and Complex Systems. Evaluation of the capacitive force between an atomic force microscopy tip and a metallic surface. 2(1):5–10, 1998.
- [33] GM Sacha, A Verdaguer, J Martinez, JJ Sáenz, DF Ogletree, and M Physics Letters Salmeron. Effective tip radius in electrostatic force microscopy. 86(12):123101, 2005.
- [34] GM Sacha, E Sahagun, and JJ A method for calculating capacitances and electrostatic forces in atomic force microscopy. 101(2):024310, 2007.
- [35] L Olsson, N Lin, V Yakimov, and R A method for in situ characterization of tip shape in ac-mode atomic force microscopy using electrostatic interaction. 84(8):4060–4064, 1998.
- [36] Th Glatzel, S Sadewasser, and M Ch Amplitude or frequency modulation-detection in kelvin probe force microscopy. 210(1-2):84–89, 2003.
- [37] OH Pakarinen, AS Foster, M Paajanen, T Kalinainen, J Katainen, I Makkonen, J Lahtinen, RM Engineering. Towards an accurate description of the capillary force in nanoparticle-surface interactions. 13(7):1175, 2005.
- [38] A Gil, Jaime Colchero, J Gómez-Herrero, and AM Baró. Electrostatic force gradient signal: resolution enhancement in electrostatic force microscopy and improved kelvin probe microscopy. *Nanotechnology*, 14(2):332, 2003.